RSC Advances

PAPER

View Article Online
View Journal | View Issue

Cite this: *RSC Adv.*, 2025, **15**, 48306

Systematical synthesis of magnetic-layered core@shell supports for metalloporphyrin immobilization aiming catalysis

Everton Henrique dos Santos, [ab] Adriana Duarte Dalla Costa, [a] Vanessa Prevot,[b] Claude Forano*[b] and Shirley Nakagaki *[a]

Received 28th October 2025
Accepted 28th November 2025

DOI: 10.1039/d5ra08288a

rsc.li/rsc-advances

Bioinspired catalytic systems based on metalloporphyrins have been extensively researched in recent years and, in many cases, have played a key role in the development of more efficient and selective catalysts. The immobilization of this family of catalyst species in robust supports can permit the preparation of recoverable and reusable catalyst solids. In this work, we present the systematic and comprehensive preparation of core@shell-like solids for catalyst immobilization based on magnetic particle, using microwave-assisted synthesis of magnetite, coated with a shell composed of two distinct LDH formulations: Mg_3Al and Ni_3Al, evaluating different LDH/magnetite molar ratios. Four different tetra-anionic metalloporphyrins (Na_4[M(TDFSPP)], M = iron(III), manganese(III), zinc(II), or magnesium(II) ions) (MP) were immobilized in both prepared LDHs. The eight resulting solids were evaluated as catalysts in the model oxidation reaction of cyclooctene to *cis*-cyclooctene oxide, using iodosylbenzene (PhIO) as the oxidant.

1 Introduction

Bioinspired catalytic systems, particularly metalloporphyrins (MPs), have been widely studied for their efficiency and selectivity.[1,2] Cytochrome P450 enzymes catalyze oxidation reactions using an ironporphyrin as the active site.[3,4] Inspiring the synthesis of MPs for diverse catalytic applications.[5–10]

However, homogeneous catalysis employing MPs face challenges such as low solubility, depends on the porphyrin structure, difficult to recover for reuse, and oxidative deactivation.[5,11] Immobilizing MPs on solid supports improves recovery, stability, and reusability, while also mitigating side reactions and solubility issues.[12–14]

Additionally, the composition and structure of the support influence catalytic performance, either through intrinsic properties or synergistic interactions with MPs, enhancing reactivity and selectivity.[14–16] In this way the research of new solids supports, and the immobilization of MPs have been investigated. Table 1 presents some examples of MP-solid catalysts investigated in different catalytic reactions.

The interaction between MP and solid supports typically occurs through covalent bonding or electrostatic interactions. Covalent bonding requires previous surface functionalization with groups like amines, for example, SBA-15 functionalized with (3-aminopropyl)triethoxysilane (3-APTS) to immobilize porphyrins.[16] In contrast, electrostatic interactions are more easily achieved by introducing residual charges on the solid surface. Layered double hydroxides (LDHs) are often used for MP immobilization due to their positively charged layers, which enhance catalytic efficiency but requires additional steps, leading to increased energy and reactant consumption.[15]

Alternatively, one of the most interesting naturally occurring candidates for solid catalyst supports is magnetite (Fe_3O_4) due to its magnetic properties and surface functionalization potential.[24–26] At high pH, its surface becomes negatively charged, allowing interaction with LDHs and other positively charged catalysts.[27,28] However, magnetite's instability, susceptibility to oxidation, and low surface area limit its direct use.[29–31] Furthermore, its small surface area further restricts its efficiency in catalytic applications, limiting direct coating with catalytic species.[32]

A core@shell approach overcoming limitations associated with bare magnetite, such as low surface area and oxidation susceptibility, while creating a more versatile and efficient catalyst system. Various materials, including silica,[33] gold,[34] ZnO,[35] TiO_2,[36] and organic polymers[37] have been used for this purpose.

LDHs are particularly attractive due to their residual positive charge, which enhances MP immobilization.[38,39] However, the typical LDH aggregation can reduce catalyst accessibility, limiting reaction efficiency.[40] To improve MP immobilization, LDH platelets can be nanostructured on spherical surfaces, reducing aggregation and enhancing catalyst stability, accessibility, and reusability.[41,42] The core@shell structure enables

[a]*Laboratório de Bioinorgânica e Catálise (LABIOINC), Departamento de Química, Centro Politécnico, Universidade Federal do Paraná (UFPR), Curitiba/PR, 81531990, Brazil. E-mail: shirleyn@ufpr.br*

[b]*Université Clermont Auvergne, CNRS, Clermont, Institut de Chimie de Clermont-Ferrand, F-63000 Clermont-Ferrand, France. E-mail: claude.forano@uca.fr*

Table 1 Examples of heterogenized MP catalysts investigated in different reactions[a]

MP	Support	Catalytic reaction	Ref.
[Mn(TPFPP)]Ac	SBA-15 mesoporous silica	*n*-Hexane oxidation	16
[Mn(TDFSPP)]Ac	Zinc hydroxide nitrate	Cyclohexane oxidation	15
$[Mn(T4MPyP)]^{5+}$ or $[Fe(TDFSPP)]^{3-}$	Zinc oxide	Cyclohexane light - assisted oxidation	17
[Co(TCPP)]	Cerium oxide nanotubes	Photo – assisted water oxidation	18
[M(TPP)] (M = Co^{2+} or Co^{3+} or Mn^{3+})	NaX zeolite	CO_2 cycloaddition to epoxide	19
[Sn(TBhBP)]	Fe_3O_4 nanoparticle	Dyes photodegradation	20
$[Co(TM4PyP)]^{4+}$	Montmorillonite	Aerobic oxidation of alcohols	21
CuPp2	Titanium oxide	4-Nitrophenol reduction	22
[Co(TSPP)]	Mg–Al LDH	Olefin epoxidation	23

[a] Where TPFPP = 5,10,15,20-tetrakis(pentafluorophenyl)porphyrin, Ac = acetate; TDFSPP = 5,10,15,20-tetrakis(2,6-difluoro-sulfonatophenyl) porphyrin; T4MPyP = 5,10,15,20-tetrakis(4-methylpyridyl)porphyrin; TCPP = 5,10,15,20-tetrakis(4-carboxyphenyl)porphyrin; TPP = 5,10,15,20-tetrakis(pheny)porphyrin; TBhBP = 5, 10, 15, 20-tetrakis (4-benzhydryl benzoate) porphyrin; Pp2 = 5,10,15,20-tetrakis[3-((carboxyl)propoxy) phenyl] porphyrin.

strong electrostatic interactions, improving catalyst performance and recovery.[43–45]

Studies on magnetite-LDH heterostructures have demonstrated high catalytic activity and easy recovery.[27,44,46–50] However, their preparation remains challenges due to the difficulty in reproducing the reported synthesis methods and controlling particle growth and size homogeneity.

In this study, we report a reproducible and systematic approach for Fe_3O_4@LDH support preparation *via* a microwave-assisted method, followed by $Mg_3Al–CO_3^{2-}$ or $Ni_3Al–CO_3^{2-}$ LDH coprecipitation coating method for four distinct iron(III), manganese(III), zinc(II), or magnesium(II) MP immobilization (Fig. 1) aiming catalytic exploration in cyclooctene oxidation.

2 Experimental section

All the reagents and solvents used in this work were purchased from Aldrich, Merck, Fluka, or Synth with analytical purity grade. Iodosylbenzene (PhIO) was prepared by hydrolysis of iodosylbenzene diacetate, according to the method described by Sharefkin and Saltzmann.[51] The PhIO purity of 93% was confirmed by iodometric titration.

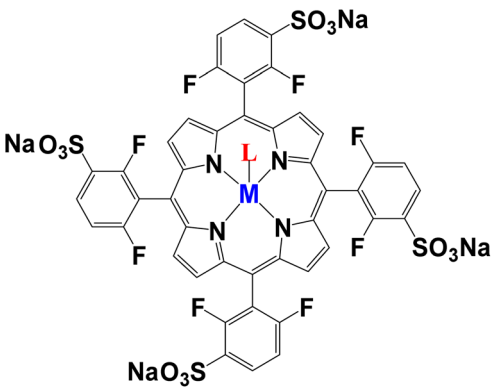

Fig. 1 Schematic representation of the structure of the generic anionic metalloporphyrin [5,10,15,20-tetrakis-(2,6-difluor-3-sulfonatephenylporphyrinate) M(II or III)] with an axial ligand (L) (L considering MnP and FeP), Na_4[M(TDFSPP)]L = MP.

2.1 Preparation of porphyrins and metalloporphyrins (MPs)

The neutral porphyrin ligand [H_2(TDFPP)] [5,10,15,20-tetrakis(2,6-difluorophenyl)porphyrin] was synthesized and purified following Lindsey's method.[52] The anionic porphyrin Na_4[H_2(TDFSPP)] [5,10,15,20-tetrakis(2,6-difluoro-sulfonatophenyl)porphyrin] tetrasodium (H_2P) was prepared through the sulfonation of [H_2(TDFPP)] using Turk's method[53] and subsequently metalated with various metal ions to form [M(TDFSPP)]L (Fig. 1).

The anionic manganese(III) porphyrin Na_4[-Mn(TDFSPP)(OAc)] (referred to as MnP hereafter) was synthesized by metalating H_2P with manganese(II) acetate tetrahydrate ($Mn(CH_3COO)_2 \cdot 4H_2O$, $Mn(OAc)_2$).[54] The iron(III), zinc(II), and magnesium(II) porphyrins (designated as FeP, ZnP, and MgP, respectively) were prepared by metalating H_2P with $FeCl_2 \cdot 4H_2O$, anhydrous $ZnCl_2$, or $MgCl_2 \cdot 6H_2O$ following Adler's method.[55] Typically, $FeCl_2 \cdot 4H_2O$ (182 mg, 0.86 mmol) was dissolved in a solution of H_2P (0.100 g, 0.086 mmol) prepared in dimethylformamide (DMF) and magnetically stirred at 300 rpm at 100 °C for 6 hours. The progress of the metalation reaction was monitored by UV-VIS spectroscopy. After completion, the solution was dried using a rotary evaporator, and the FeP solid was purified *via* column chromatography on Sephadex G10, using water as the eluent. The purified solid was dried in a rotary evaporator and stored at room temperature (FeP: 50.4 mg, yield 47%; ZnP: 498.6 mg, yield 90%; MgP: 43 mg, with 83% yield reported for ZnP and MgP when 50 mg of H_2P was used). UVVIS spectrum bands λ_{max} (nm, ethanol, concentration solution *ca.* 1×10^{-5} mol L^{-1}): FeP: 388 (Soret band, $\varepsilon = 1.3 \times 10^4$ L mol^{-1} cm^{-1}) ZnP: 417 (Soret band, $\varepsilon = 7.7 \times 10^4$ L mol^{-1} cm^{-1}), MgP: 423 (Soret band, $\varepsilon = 2.2 \times 10^4$ L mol^{-1} cm^{-1}) and MnP: 460 (Soret band, $\varepsilon = 4.6 \times 10^4$ L mol^{-1} cm^{-1}). The IR spectra of the MPs exhibited similar bands to those of H_2P, with the notable absence of the shoulder bands around 3300 and 1600 cm^{-1}, corresponding to the N–H stretching and deformation modes. Additionally, for MnP, characteristic bands at

1539 and 1382 cm^{-1} were observed, associated with the C–O stretching modes of the acetate group.

2.2 Preparation of microwave-assisted solvothermal magnetite (M)

The magnetite (M) was synthesized *via* a solvothermal route,[56] adapted for a microwave reactor instead of a conventional oven. A solution of 25 mL of ethylene glycol containing $FeCl_3 \cdot 6H_2O$ (0.1292 mol L^{-1}), sodium acetate (1.096 mol L^{-1}), and polyethylene glycol (PEG 1000 or 10 000–2.5 × 10^{-3} mol) was prepared at 50 °C and stirred magnetically for approximately 15 min. The solution was transferred to a microwave quartz reactor equipped with magnetic stirring. The reaction was carried out under determined time and temperature conditions, as detailed in Table 2. Later, the solid was recovered using a neodymium magnet, washed three times with 20 mL of water and three times with 20 mL of ethanol, and left to dry for *ca*. 16 hours at room temperature. Typical yield of 100% to the optimal condition was achieved (*ca*. 250 mg).

2.3 Preparation of core@shell structures (M7/LDH) containing magnetite (M7) and layered double hydroxide (LDH)

The magnetite (M7) (200 °C, 2 h) was coated with LDH using a coprecipitation method,[57,58] following optimized LDH/M ratios, systematically calculated in this work based on the difference between a sphere of 220 nm volume and another of 200 nm. For a 0.6 ratio, 120 mg of magnetite M7 was dispersed in 100 mL of distilled water in a 500 mL round-bottom reactor with ultrasound bath assistance for 10 minutes. Then, a mixed metal nitrate solution (9.36 × 10^{-3} mol L^{-1} Mg^{2+}or Ni^{2+}/3.12 × 10^{-3} mol L^{-1} Al^{3+}) and base solution (6.03 × 10^{-3} mol L^{-1} Na_2CO_3/0.01 mol L^{-1} NaOH) were added simultaneously to maintain a constant pH of 10.0, using peristaltic pumps.

The addition took ~6 hours at room temperature. The solid was recovered using a neodymium magnet, washed with water and ethanol (3 times each), and dried for 16 hours at room temperature. The Mg/Al and Ni/Al LDH-coated solids were labeled as M7@MA-*n* (for MgAl LDH at magnetite (M7) solid) and M7@NA-*n* (for Ni/Al LDH at magnetite (M7) solid), with *n* value denoting the LDH/M7 molar ratio used in the preparation of the LDH (*e.g.*, M7@NA-6 for molar ratio of LDH/M7 = 0.6).

Table 2 Solids prepared through microwave-assisted solvothermal route

Obtained solid	Temperature (°C)	Time (h)
M1 and M2	100	0.5 and 1
M3 and M4	150	0.5 and 1
M5 to M14[a]	200	0.5, 1, 2, 3, 4, 5 and 6

[a] Microwave-assisted solvothermal reactions were performed in a Discover SP-D CEM 300 watt magnetron reactor at 200 °C for different reaction times involving 0.5 to 6 h. Some experiments were done in duplicate.

Pure Mg/Al and Ni/Al LDHs were prepared similarly, without the presence of magnetite M7 (Table SI 1, SI).

2.4 Immobilization of MPs on core@shell solids

The MPs were immobilized on M7@MA-6 and M7@NA-4 solids *via* electrostatic self-assembling, as previously reported.[13–15,58] Typically, in a 100 mL round-bottom flask, FeP (50 mL of *ca*. 2.0 × 10^{-5} mol L^{-1} ethanol solution) and 0.100 g of M7@MA-6 or M7@NA-4 were stirred mechanically at 300 rpm and 25 °C for 5 hours, forming a brown mixture. The FeP-loaded solid was recovered using a neodymium magnet and exhaustively washed with ethanol until the Soret band of FeP was no longer detected in the UV-Vis spectrum of the supernatant, confirming the absence of leaching.

The resulting materials were designated as M7@MA@FeP and M7@NA@FeP and dried at 25 °C for two days. The immobilization efficiency (loading), expressed as mol of FeP per gram of support, was determined indirectly through UV-VIS analysis of the supernatant.

The ZnP-loaded solids were designated as M7@MA@ZnP and M7@NA@ZnP, the MgP-loaded solids as M7@MA@MgP and M7@NA@MgP, and the MnP-loaded solids as M7@MA@MnP and M7@NA@MnP. All materials were characterized by powder XRD, FTIR, and UV-VIS.

2.5 Catalytic reactions

The prepared solids based on M7@MA-6 and M7@NA-4, each containing one of the four MPs (FeP, MnP, ZnP, or MgP), were preliminarily evaluated as catalysts in the oxidation of cyclooctene using PhIO as the oxidant, yielding *cis*-cyclooctene as the sole product.

2.6 Cyclooctene oxidation

All cyclooctene oxidation reactions followed the same protocol,[13,15,16] using a 1 : 20 : 2000 ratio of MP/PhIO/cyclooctene. In a 2.0 mL amber glass vial with a polypropylene screw cap and PTFE/silicone septa, *ca*. 5 mg of M7@MA@MP or M7@NA@MP, *ca*. 0.4 mg of PhIO (2 × 10^{-6} mol) as the oxidant, 500 μL of acetonitrile (ACN) as solvent, and *ca*. 26 μL of cyclooctene (2 × 10^{-4} mol) were added. The mixture was stirred at 300 rpm using a glass-covered magnetic stir bar at 25 °C for 1 hour, under an argon atmosphere and protected from light.

After the reaction, 100 μL of saturated sodium sulfite in ACN and 200 μL of methanol were added to dissolve and quench excess PhIO. The solid catalyst was recovered using a neodymium magnet and washed three times with 100 μL of ACN. The supernatants from the reaction and washes were combined in a 2.0 mL volumetric flask. For product quantification, 30–50 μL of *n*-octanol (internal standard, 1 × 10^{-2} mol L^{-1}) was added to 500 μL of the reaction solution, and the *cis*-cyclooctene product was quantified by gas chromatography, performed in duplicate, with yields based on the initial PhIO amount. All reactions were carried out at least in duplicate.

Control reactions for heterogeneous catalysis were conducted in the same experimental conditions, using as catalyst

the solids M7, Mg_3Al-LDH, Ni_3Al-LDH, M7@MA-6 or M7@NA-4 with PhIO. For reactions using non-magnetic solids, recovery was performed by centrifugation at 4000 rpm for 10 minutes. Homogeneous catalysis was also tested using free MPs instead of immobilized ones. The control reaction for homogeneous catalysis was performed with PhIO and substrate under the same experimental conditions.

2.7 Characterization and apparatus

Powder X-ray Diffraction (XRD) patterns were recorded using Shimadzu XRD-7000 and PANalytical X'Pert PRO diffractometers, operating at 30 kV and 40 mA (Cu Kα radiation, $\lambda = 1.5418$ Å). Measurements were taken from 3–80° (2θ) with a 2° min^{-1} scan rate. *In situ* temperature controlled XRD patterns were recorded from 25 to 1000 °C. Fourier transform infrared spectroscopy (FTIR) spectra (400–4000 cm^{-1}) were collected on a VERTEX spectrophotometer using KBr pellets with 1% (m m^{-1}) solid. Ultraviolet-visible spectroscopy (UVVIS) absorbance spectra were obtained in the range 200–800 nm with HP 8452A and Varian Cary 100 spectrophotometers. Transmission electron microscopy (TEM) analysis was performed with JEOL-JEM 1200 and JEOL-JEM-2100plus microscopes at 120 kV. Scanning electron microscopy (SEM) images were recorded with Tescan VEGA3 LMU and ZEISS SUPRA 55VP microscopes. Nitrogen adsorption–desorption isotherms were obtained with a Micromeritics ASAP 2020 and BET surface areas were calculated. Samples (80 mg) were degassed under vacuum at 80 °C for 10 h. TGA/DSC analysis was conducted using a Mettler Toledo DSC 1 STARe and SETSYS Evolution TG-ATD DSC, from 20–1000 °C at 10 °C min^{-1} under N_2 atmosphere. Reaction products were quantified using an Agilent 6850 GC with a DB-WAX capillary column and flame ionization detector.

3 Results and discussion

3.1 Systematic synthesis and characterization of core@shell materials

Magnetite (M) was synthesized using a microwave-assisted solvothermal route in a digestion microwave reactor, as an alternative to the traditional polyol-based solvothermal method.[56] The conventional polyol route presented challenges in achieving uniform particle size distribution, size control, and synthesis time optimization, which hindered the formation of the desired magnetite-based core@shell structure in this work.

To address these limitations, in this work microwave-assisted synthesis was explored, as it has been reported to enable magnetite production.[59,60] However, prior studies typically employed mild temperatures and short reaction times, resulting in small particle sizes,[61,62] or large particles under high-pressure conditions.[63]

This study systematically investigated reaction temperatures of 100 °C, 150 °C, and 200 °C, with reaction times of 0.5 and 1 hour. At 200 °C, reaction durations were extended from 2 to 6 hours to determine optimal conditions. Further optimization included varying the molecular weight of polyethylene glycol (PEG 1K and 10K) or on its absence. Iron salt concentrations of 0.13 and 0.26 mol L^{-1} were also evaluated, under autogenous pressure.

For temperatures below 200 °C and reaction times not higher than 1 h (M1 to M6) (Table 2), magnetite is not formed as confirmed by the powder XRD patterns (Fig. SI-1). Instead, amorphous unidentified phases are observed for M1 to M4, while M5 and M6 show a mixture of α-FeOOH and ($Fe_2O(CH_3COO)(OH)_3 \cdot H_2O$) consistent with data reported in the literature.[32]

Based on these preliminary results, effect of reaction time from 2 h to 6 h was explored at 200 °C, yielding solids M7 to M11, respectively (Table 2). All samples (M7–M11) exhibited similar PXRD patterns (Fig. 2A) with peak positions at 2θ = 18.4°, 30.3°, 35.5°, 37.0°, 43.4°, 53.6°, 57.0°, and 62.0°, corresponding to the (111), (220), (311), (222), (400), (422), (511), and (440) crystal planes of magnetite.[32,56] The size of the crystalized domains calculated using Scherrer's equation (Fig. SI-2), remained constant, in the range of 13–19 nm.

Since the structural data of M7 to M11 samples showed no significant differences, the conditions used for M7 were chosen for further tests. These included examining the effect of PEG molecular weight, typically PEG-1K and PEG-10K (M12 and M13 respectively) and higher iron salt concentration, (M14). The results confirm that all tested conditions are effective for synthesizing magnetite using the proposed microwave-assisted method.

Increasing the Fe^{3+} initial concentration has the most effective effect on the particle size (35 nm). The addition of PEG inhibited crystal growth, reducing the size of Fe_3O_4 nanospheres to an average diameter of 11 nm and promoting polydispersity. Notably, varying the PEG molecular mass between 1K and 10K had a negligible effect.[64] This behavior aligns with the traditional LaMer mechanism.[65]

When crystal growth is governed by surface reactions rather than diffusion, surface reactivity decreases as the crystal size increases, thereby slowing further growth. Consequently, nucleation competes with crystal growth, leading to the formation of new nuclei, which contributes to both polydispersity and a reduction in overall crystal size. This phenomenon is confirmed by TEM analysis (Fig. 2B–H).[65]

The spectrum for magnetite M7 shown in Fig. 2B shows bands at 3500 and 1630 cm^{-1} correspond to stretching and bending modes of adsorbed water or hydroxyl species, including those coordinated to surface iron sites in magnetite. The band at 2922 cm^{-1} arises from asymmetric –C–H stretching, likely due to residual organic precursors. The feature at 1410 cm^{-1} is assigned to the C–O ν_3 mode, indicating adsorbed CO_2/CO_3^{2-} from atmospheric exposure, polyol (EG/PEG), or acetate used during synthesis. Bands at 628, 580, and 437 cm^{-1} are characteristic of Fe in tetrahedral and octahedral coordination within the magnetite lattice.

The TEM images for solids M7, M11, and MAGW14 are shown in Fig. 2B–H. For M7, synthesized in 2 hours (Fig. 2B and C), more homogeneous spherical particles with a mean diameter of *ca*. 200 nm are observed than the M11 particles (Fig. 2D and E), prepared after 6 hours of reaction, exhibit less size homogeneity, and smaller average particle size compared to

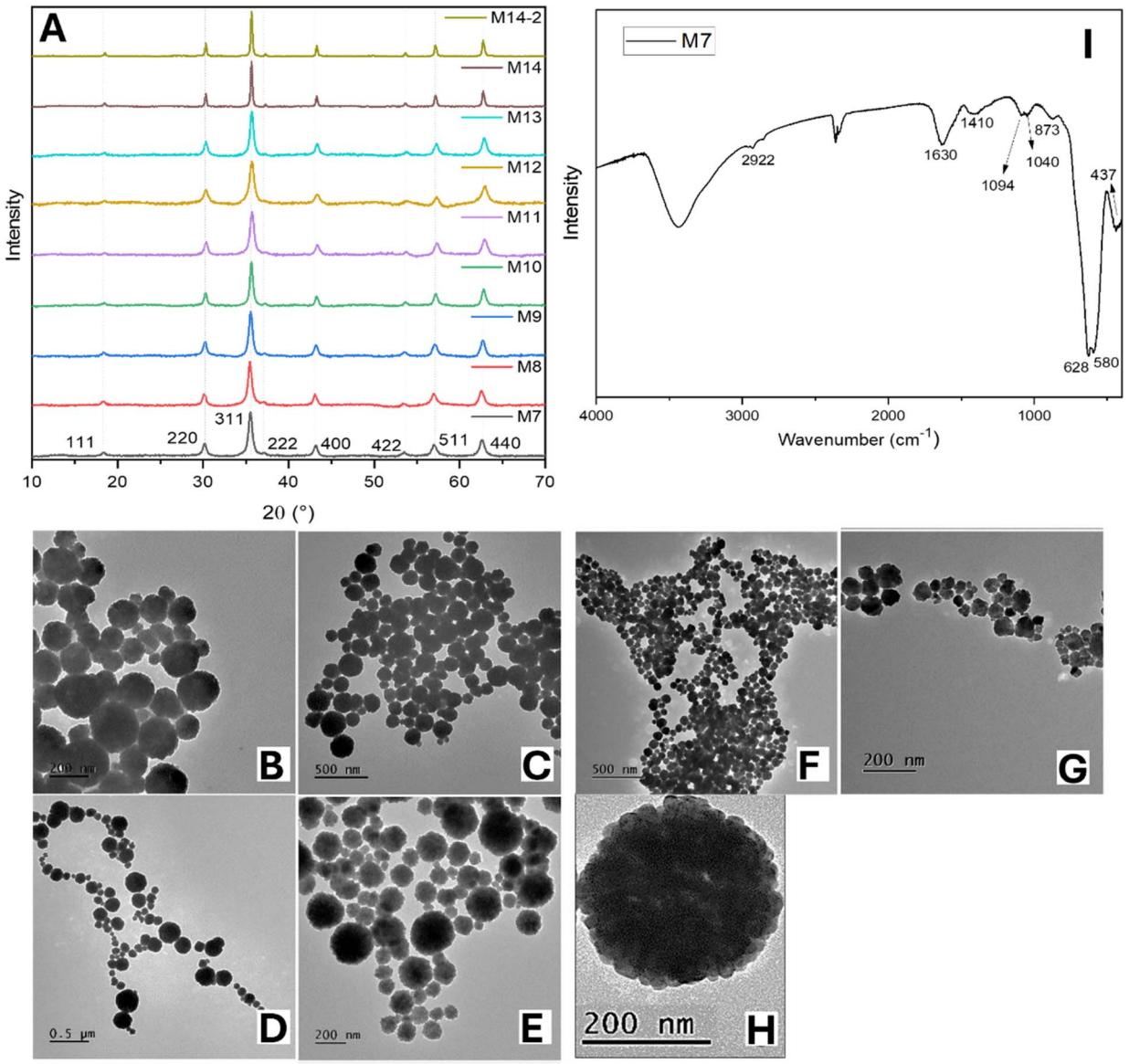

Fig. 2 (A) Diffractograms of solids M7 to M14 prepared by microwave-assisted solvothermal route, TEM images of the solid M7 (B and C), M11 (D and E), M14 (F and G), (H) magnification of a sphere of the solid M7 and (I) FTIR spectrum of the solid M7.

M7, likely due to secondary nucleation events, consistent with the LaMer mechanism.[65] These events lead to a smaller average particle size compared to M7.

In the case of M14, the average particle size is approximately 50 nm, suggesting insufficient time for complete particle growth, indicating the need for extended reaction times. Upon closer examination of the M7 particles (Fig. 2H), the spherical particles display a raspberry-like structure, composed of aggregated smaller nanoparticles ranging from 5 to 10 nm in size. This aggregation justifies the Scherrer-derived crystallite size (*ca*. 15 nm), as these smaller spheres likely correspond to individual crystallites. The SEM images of M7 (Fig. SI 3) confirm the particle size homogeneity and the raspberry-like structure observed in the TEM analysis. These findings suggest that particle growth in the microwave-assisted solvothermal route proceeds predominantly through the aggregation of primary nanoparticles rather than Ostwald ripening,[66] with higher surface energy stabilized by the formation of particle conglomerates.[32,59,67]

The magnetite reported here was prepared at least four faster when compared to traditional routes.[56,68] Due to its higher particle size homogeneity, the M7 solid was selected for further characterization and core@shell preparation studies.

HTK-XRD analysis of the M7 solid (Fig. SI 4) revealed structural changes with increasing temperature. At 500 °C, the conversion of magnetite (Fe_3O_4, JCPDS 19-629) and/or maghemite (γ-Fe_2O_3, JCPDS 39-1346) to hematite (α-Fe_2O_3, JCPDS 86-055) becomes evident by the appearance of peaks at $2\theta = 33.1°$ (104) and 53.98° (116), which intensify up to 1000 °C, consistent with the loss of magnetism.[69–71] Differentiating magnetite and

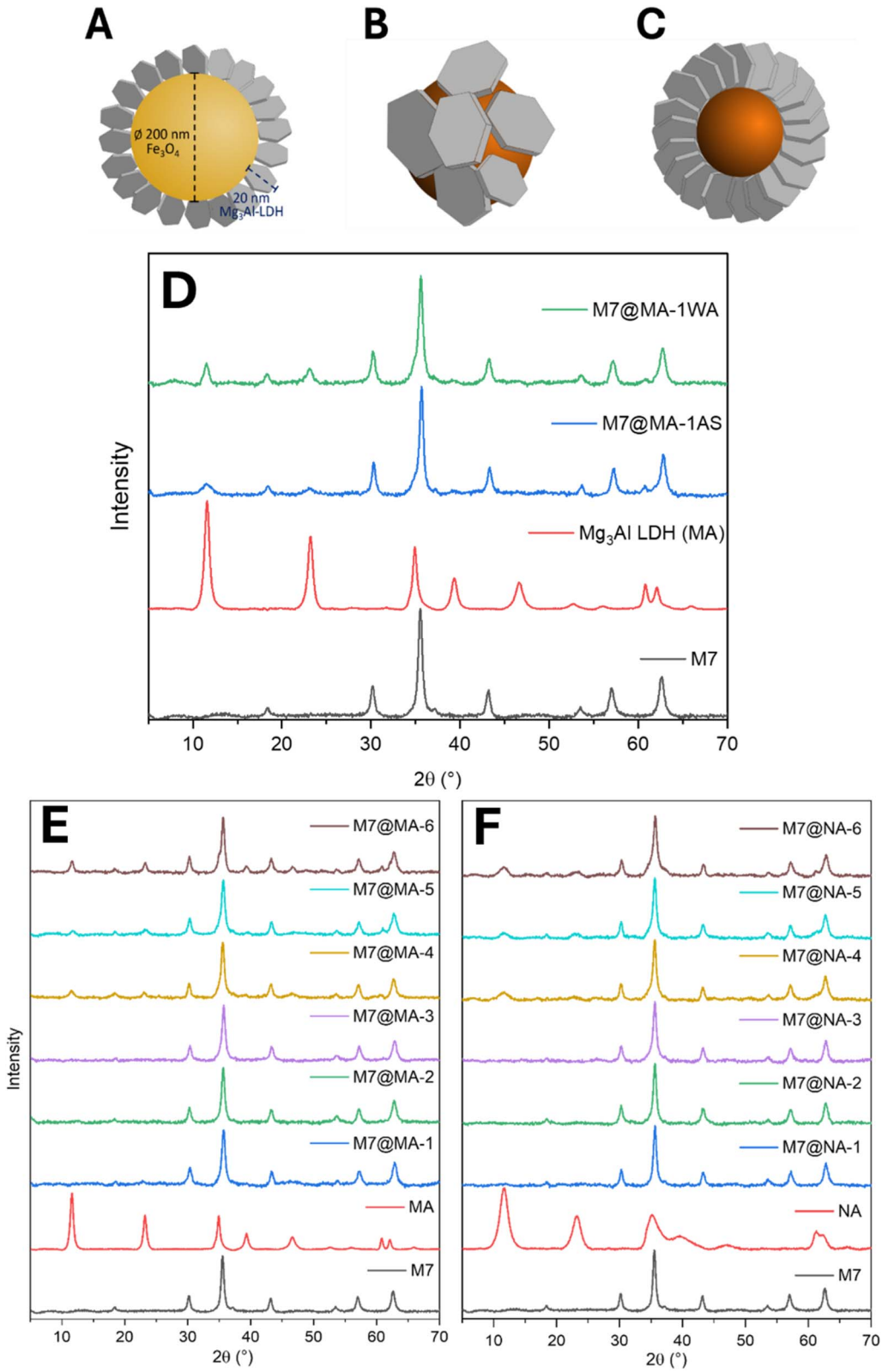

Fig. 3 Idealized core@shell solid representation with 200 nm core and 20 nm shell sizes (A) and representation of LDH/magnetite assemblies for M7@MA-6 (B) and M7@NA-4 (C), (D) diffractograms for core@shell prepared by the proposed route using the solid M7 as core and Mg3Al-LDH (MA) as shell and the diffractograms for core@shell solids prepared varying the LDH/magnetite molar ratio from 0.1 to 0.6, for the MA-LDH (E) and NA-LDH (F) series.

maghemite by XRD is difficult due to their similar cubic structures,[72] though magnetite has more Fe^{2+}, which oxidizes to Fe^{3+} in maghemite.[69,70] In air, magnetite often forms core@shell particles with a magnetite core and maghemite shell.[69–71,73]

TGA and TGA/MS analyses (Fig. SI 5A and B) show an initial mass loss from adsorbed water, followed by the release of structural water from hydroxyl groups in magnetite. A third, unexpected mass loss occurs between 600–700 °C—where a mass gain is typically expected due to full oxidation of Fe^{2+} to Fe^{3+} and the conversion to α-Fe_2O_3.[69–71] TGA/MS (Fig. SI 5B) reveals CO_2 release in this range, likely from trapped organic precursors released during particle coalescence and phase transition to hematite.

M7 was characterized by FTIR spectroscopy, with the spectrum shown in Fig. 2I. The characteristic Fe–O bands were observed at 628 cm^{-1} for iron in a tetrahedral environment, and at 580 and 437 cm^{-1} for iron in an octahedral environment, consistent with the inverse spinel structure of magnetite.[73,74] Bands at 3500 and 1630 cm^{-1} indicate the presence of adsorbed water molecules and surface hydroxyl groups. Additionally, bands at 2922 and 1410 cm^{-1} correspond to C–H and C–O vibration modes, likely originating from organic precursor residues, in agreement with the third mass loss event observed in the TGA analysis (Fig. SI 5). Vibration bands at 1040 and 1094 cm^{-1} are typical of vC–O symmetric and asymmetric stretching vibration of ethylene glycol, as that at 1410 cm^{-1}.[75]

3.2 Synthesis and characterization of Fe_3O_4@LDH core–shell assembly

As reported in the,[27,44,46–50] attempts to synthesize pure and homogeneous particles of Fe_3O_4@LDH core–shell structures were often limited by side coprecipitation of LDHs. To address this, we proposed using standard particle dimensions, specifically a 20 nm LDH shell surrounding a 200 nm Fe_3O_4 core (Fig. 3A). This approach resulted in a theoretical LDH-shell to magnetite-core volume ratio and molar ratio of respectively 0.1 and 0.3.

The influence of the aging step (AS)[66] was evaluated by comparing aged (M7@MA-1AS, 16 h) and non-aged (M7@MA-1WA) samples, with MA-LDH as a reference. These solids were characterized by powder XRD (Fig. 3D).

Both M7 and MA diffraction patterns appeared in M7@MA-1AS and M7@MA-1WA, even after washing and magnetic recovery, confirming strong interaction between magnetic and layered solids. The M7@MA-1AS diffractogram showed a weaker 00l peak than M7@MA-1WA, suggesting lower LDH content or reduced crystallinity in the aged sample. The lower content then led to a weaker intensity for structural LDH peaks towards the magnetite diffraction peaks.

SEM and TEM analyses (Fig. 4) further clarified these differences. Small hexagonal, delaminated LDH platelets (<100 nm) were observed (Fig. 4A and B), consistent with expected morphology. Without aging (Fig. 4E and F), LDH formed a more extensive coating on magnetite, whereas aging (Fig. 4C and D) led to partial detachment. This results from Ostwald ripening,[66] where smaller LDH particles dissolve and grow into larger ones.

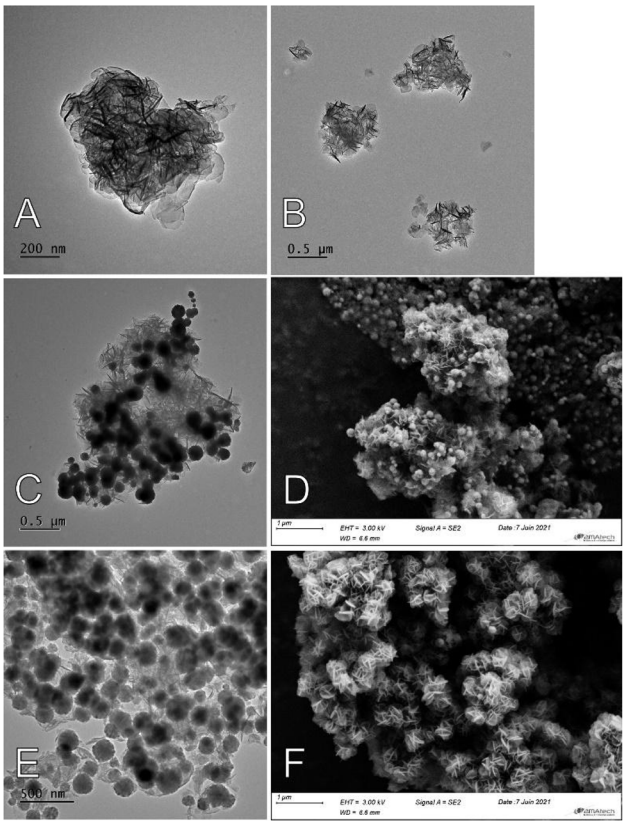

Fig. 4 TEM images for the solids MA (A and B), M7@MA-1AS (C), M@MA-1WA (E), besides SEM images for core@shell solids M7@MA-1AS (D) and M@ MA-1WA (F).

These findings align with the XRD results, confirming fewer LDH particles in M7@MA-1AS. Therefore, the synthesis without aging was selected for further studies.

The range of 0.1 to 0.6 LDH/magnetite ratios was explored for both Mg_3Al–CO_3^{2-} LDH (MA) NiAl–CO_3^{2-} LDH. Diluted salt and base solutions ($\sim 10^{-3}$ mol L^{-1}) and slow salt addition rate (0.33 mL min^{-1}) were used to prevent large particle formation. The pH was kept at 10 to optimize LDH formation[57,58] and promote hydroxyl deprotonation on the magnetite surface,[27,50] enabling electrostatic interactions with positively charged LDH layers.[13] Room temperature ensured mild synthesis conditions.

Therefore, the solids were prepared with constant salt and base concentration, just increasing the volume of salt solution (volume mL/molar ratio): 16.6/0.1, 33.3/0.2, 50/0.3, 66.6/0.4, 83.3/0.5 and 100/0.6 (resulting solids named by M7@MA-1 to M7@MA-6 and M7@NA-1 to M7@NA-6 – Table SI 1).

The MA and NA LDHs were chosen based on different ways of interaction to magnetite surface, since NA particles can grow perpendicular to the surface,[50] while MA hexagons commonly interact parallel to the spherical surface.

The XRD diffractograms for the MA and NA LDHs, M7, and the M@MA and M@NA series are shown in Fig. 3E and F, respectively. The MA and NA LDHs exhibit characteristic peaks at 2θ: 11.5° (003), 23.2° (006), 34.9° (012), 38.9° (015), 46.5° (018), 61.0° (110), 62.06° (113), and 65.8° (116). The peaks for MA LDH solids (Fig. 3E) are more intense and defined than

those for NA LDH solids (Fig. 3F), indicating higher crystallinity for the MA LDH solids.[76,77]

The calculated *d*-spacing using Bragg's equation for both LDHs yielded values of 7.63 and 7.62 Å, consistent with intercalated CO_3^{2-} anions, as expected due to the lack of atmosphere control.[76] For both LDHs, the a_0 cell parameters, determined from the (110) peaks at 60.79° and 61.39° (2θ) for MA and NA, respectively, are 3.045 Å for MA and 3.018 Å for NA. These values align with the 3 : 1 M^{2+}/M^{3+} ratio used in the synthesis.[77]

For the core@shell solids, characteristic LDH peaks (003 and 006) are observed at 11.63° and 23.26° for MA LDH solids, and at 11.70° and 23.22° for NA LDH solids. Additionally, the (110) peak, near 60° (2θ), appears in both core@shell structures when the LDH/magnetite ratio is 0.4 or higher. These results are consistent with the presence of LDHs with hexagonal morphology,[78–81] and the peak intensities increase with ratios up to 0.6, confirming the layered structure alongside the magnetic phase.

The solids containing Mg_3Al LDH (M7@MA-1, M7@MA-3, and M7@MA-6) and Ni_3Al LDH (M7@NA-2, M7@NA-4, and M7@NA-6) were characterized by SEM, as shown in Fig. 5A–F.

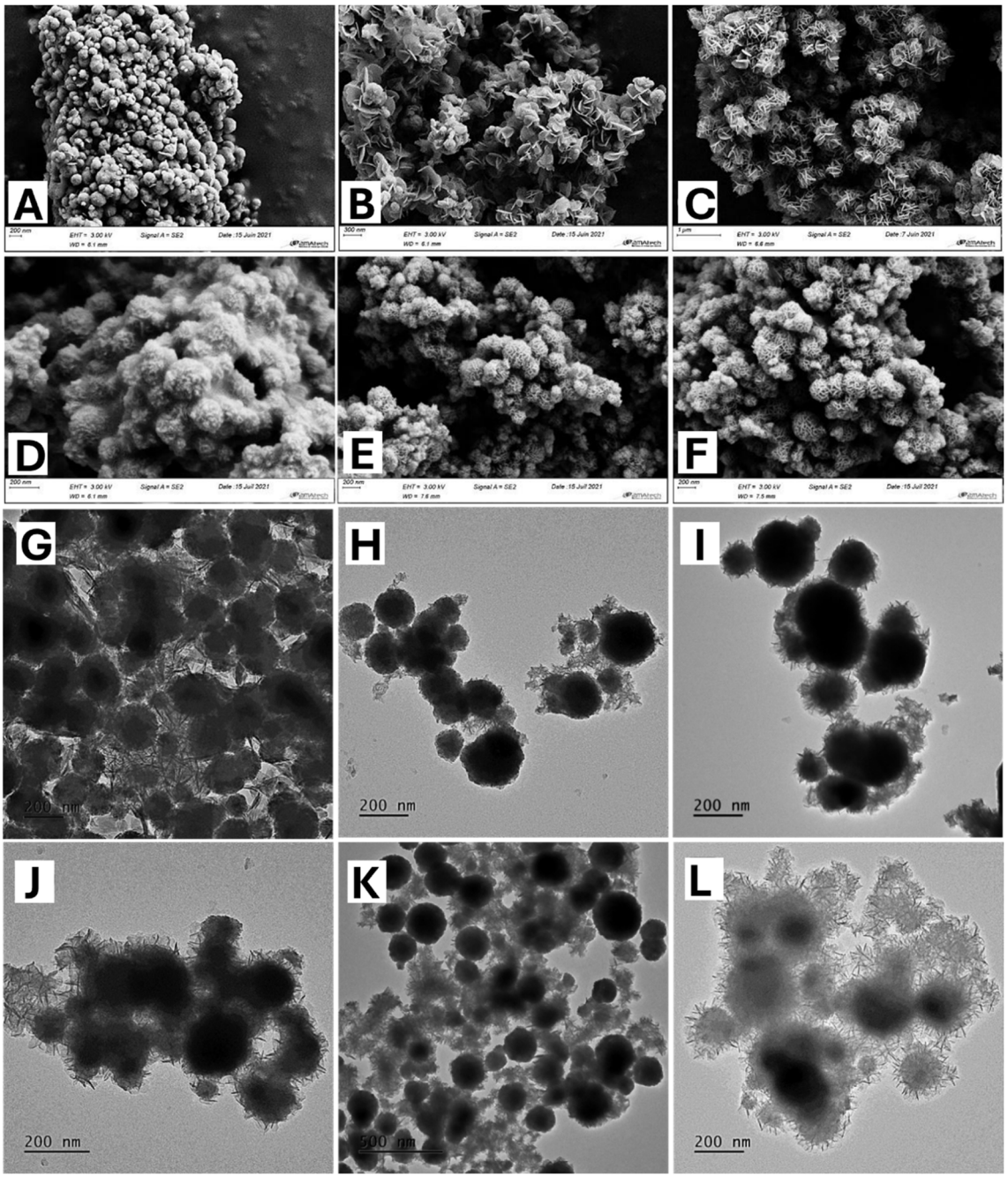

Fig. 5 SEM images of the solids M7@MA-1, M7@MA-3 and M7@MA-6 (A–C, respectively), M7@NA-2, M7@NA-4 and M7@NA-6 (D–F, respectively) and TEM images for solids M7@MA-6 (G), M7@NA-1 (H), M7@NA-3 (I) e M7@NA-4 to M7@NA-6 (J–L, respectively).

In the MA-LDH series (Fig. 5A–C), increasing the LDH/magnetite ratio resulted in progressively greater coverage of the magnetite particles. Well-defined hexagonal LDH particles were also observed. These results align with the XRD patterns, indicating that a 0.6 ratio (solid M7@MA-06) provides optimal coverage of the magnetite particles with MA-LDH.

In the NA-LDH series (Fig. 5D–F), the magnetite surface was coated even at the lowest LDH/magnetite ratio. However, no distinct LDH particles were observed at a 0.2 ratio. Both the 0.4 and 0.6 molar ratios (solids M7@NA-4 and M7@NA-6, respectively) provided good interaction and core coverage, yielding similar results. Based on the XRD patterns, a 0.4 molar ratio appears to be optimal, as it minimizes the formation of excess NA-LDH particles and enhances the visibility of the layered material. Unlike the MA-LDH series, the SEM images suggest that the NA-LDH particles are less well-defined.

The TEM images for the solids M7@MA-6, M7@NA-1, M7@NA-3, M7@NA-4, M7@NA-5, and M7@NA-6 are presented in Fig. 5G–L.

Fig. 5G shows magnetic particles enclosed within layered solid platelets, supporting the hypothesis that MA-LDH platelets form separately from the magnetite but, due to synthesis conditions (such as pH and mechanical stirring), align parallel to the magnetic core surface through electrostatic interactions. Notably, the layered material was only observed in combination with the magnetite, never independently, further validating this hypothesis.

In contrast, the NA-LDH series suggests a potential covalent interaction with the magnetite. $NiFe_2O_4$ ferrites, which are spontaneously formed through Ni–O–Fe bonds, are known to occur *via* multiple routes.[82–84] Although the magnetic particles here are pre-synthesized, oxo-bridges could still form at the surface, creating a coordinative environment similar to ferrites. This interaction may result in a nickel ion layer, where Ni^{2+} ions act as seeds for LDH nucleation and growth. Consequently, the NA-LDH platelets align perpendicularly to the magnetite cores, as observed in Fig. 5H–L, consistent with literature reports.[27,44,46–50] The solids M7@MA-6 and M7@NA-4 were selected for further study.

Based on observations from SEM and TEM images for the chosen solids M7@MA-6 and M7@NA-4, the proposed interaction between layered and magnetic solid is schematically represented on Fig. 5B and C respectively.

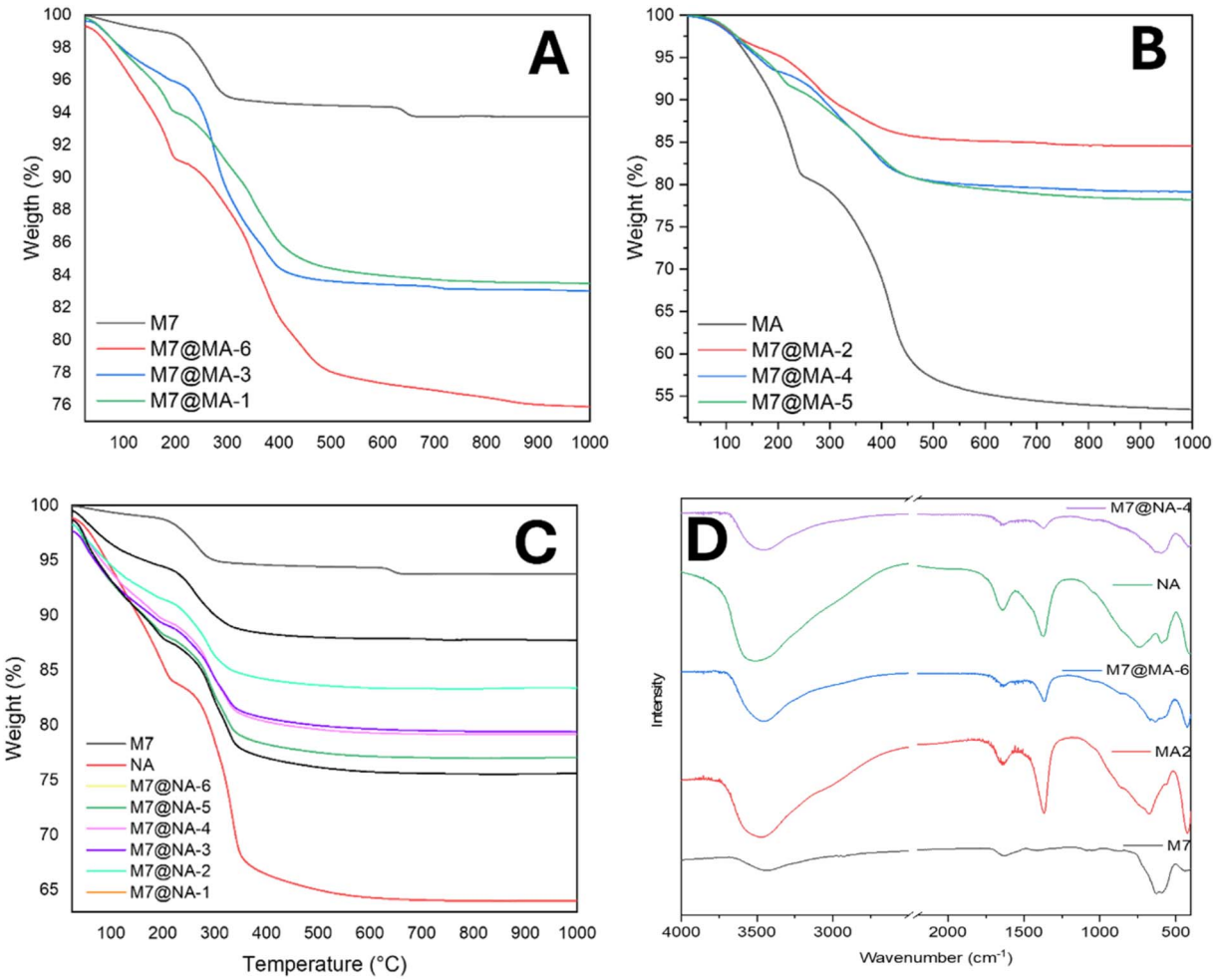

Fig. 6 TGA graphics for core@shell solids containing MA LDH (A and B), core@shell solids containing NA LDH (C) and FTIR spectra for core@shell solids, besides the MA and NA LDHs and M7 (D).

The TGA analysis of these solids, from 30 to 1000 °C (Fig. 6A–C) reveals two predominant and different mass loss events. The first one is related to adsorbed water molecules on solids surface, followed by structural hydroxyl and water molecules removing from LDH structure, up to 200 °C, and the last one associate to the full conversion to the metal oxides from layered structure.[76] The increase on the LDH/magnetite ratio intensify the mass loss of each event, as expected. It worth to highlight that the full conversion of magnetite to hematite does not occur on core@shell structure, and even after reaching 1000 °C, the core@shell solids keep the magnetic susceptibility, no matter the ratio LDH/magnetite used.

A mass loss of 45% was observed for the MA solid (Fig. 6A and B) and 35% for the NA solid (Fig. 6C), with two distinct mass loss events as temperature increased. The first event, around 200 °C, corresponds to the dehydration of adsorbed water from the interlayer domain, followed by complete conversion to metal oxides starting at 250 °C.[46,76]

The observed mass loss aligns with the powder X-ray diffraction results for both MA and NA LDH-containing solids. As the proportion of LDH in the hybrid solid increases, the mass loss also increases. The following observed mass losses were recorded from TGA, based on ascending LDH/magnetite molar ratios: MA-LDH 10%, 9%, 10%, 14%, 15%, and 18%. For NA-LDH hybrids: 6%, 10%, 13.6%, 14%, 16%, and 18%.

These percentages were normalized excluding the 7% mass loss attributed to magnetite structure. Minor discrepancies in these values may arise from operational errors but remain consistent with the increasing LDH/magnetite ratios. The mass loss corresponds to the decomposition of the LDH component, with complete calcination forming metal oxides.[76] Notably, even at the lowest LDH ratio, the layered solid interacts with the magnetite, as the final product retains magnetic properties, unlike isolated M7.

When the experimental mass loss is compared to the theoretical amount of LDH employed (Table SI 1) and hematite is considered the final oxidation product of magnetite, the average experimental mass loss is 12.6% relative to the theoretical value, with a standard deviation of 2.3%. These consistent values suggest that the experimental LDH/magnetite ratios closely match the predicted ratios. Any relative error is likely due to phase transitions in the magnetite core, with the hematite phase used as a reference in the calculations.

HTK-XRD analysis was performed for solids with 0.3 and 0.6 LDH/magnetite ratios for both M@MA and M@NA (Fig. SI 4B–E).

In the core@shell structures (Fig. SI 4B–E), the transition from magnetite/maghemite to hematite was delayed at a 0.3 ratio and completely inhibited at 0.6, indicating that LDH oxides form instead of magnetite. During this process, metal oxides interact with magnetite, preventing oxidation and preserving magnetism up to 1000 °C.[85] The nickel–aluminum LDH in the M7@NA series (Fig. SI 4D and E) provided stronger protection, even at a 0.3 molar ratio. This supports the hypothesis that NA-LDH interacts more effectively with magnetite through covalent bonding between nickel and iron, mediated by oxo bridges.

Table 3 BET calculated parameters for M7, MA, NA, and core@shell solids

Solid	Specific surface area ($m^2\ g^{-1}$)	Pore size (nm)	Pore volume ($cm^3\ g^{-1}$)
Magnetite[56]	31.0	1.9	0.14
M7	45.57	13.03	0.14
MA	101.63	12.40	0.31
M7@MA-6	84.46	22.04	0.46
NA	75.58	27.67	0.52
M7@NA-4	103.50	12.17	0.31

Since M7@MA-6 and M7@NA-4 were selected for further study, N_2 gas adsorption–desorption analyses were performed on M7 and on both MA and NA-LDHs, as well as on M7@MA-6 and M7@NA-4 (Fig. SI 6). All solids exhibited type-IV isotherms with type-III hysteresis, characteristic of slit-like pores, consistent with previous reports in the literature.[32,47]

Using the BET method, surface area, pore size, and pore volume were determined (Table 3), with values consistent for hybrid solids.[44,46,47] All solids exhibited mesoporosity, including M7 alone, due to the aggregation of small crystallites during magnetite formation, increasing the porous size from 2 to 13 nm and directly reflecting on a surface area increase when compared to traditional solvothermal route.[56] The core@shell solids show increased surface area compared to M7, attributed to the small LDH particles on the surface.[44,46,47] For M7@MA-6, the surface area decreases due to the parallel alignment of MA-LDH platelets with magnetite. In contrast, M7@NA-4 exhibits higher surface area, likely due to the perpendicular growth of smaller NA-LDH particles, which reduces aggregation and increases exposed surface.

Fig. SI 7 illustrates the pore size distribution calculated using the BJH method.[86] For magnetite M7 (Fig. SI 7A), the pore size is centered at 2.08 nm, extending up to 20 nm, typical of mesoporous materials. A similar pattern appears in the core@shell solids. In M7@MA-6 (Fig. SI 7C), the pore size distribution broadens compared to the MA solid (Fig. SI 7B), likely due to the layered hydroxide surrounding the magnetite, resulting in heterogeneity.

In contrast, NA-based solids exhibit narrower distributions. Without magnetite (Fig. SI 7D), the pore size ranges from 5 to 150 nm, peaking at 28 nm. When interacting with magnetite (Fig. SI 7E), the pore size narrows to 3–50 nm, suggesting a more organized structure, as confirmed by TEM images (Fig. 5).

In summary, the BJH and BET analyses (Table 3) indicate that the M7@MA-6 solid displays greater porosity, with a wider range of pore sizes and volumes successfully obtained with a proposed, reproducible and improved mild condition method compared to already reported core@shell solids.[46,49,87,88] This feature may enhance the immobilization of metalloporphyrin complexes, directly improving interactions with substrates in catalytic applications.

M7@MA-6 and M7@NA-4 were characterized by Fourier-transform infrared spectroscopy (FTIR), with their spectra compared to those of the precursors M7, MA, and NA (Fig. 6D).

The MA and NA LDH spectra show broad bands between 3600–3200 cm^{-1}, attributed to O–H stretching from the LDH structure and adsorbed water, further supported by the O–H deformation band at 1650 cm^{-1}. A band at 1368 cm^{-1} corresponds to the asymmetric C–O vibration of intercalated carbonate anions, consistent with the *d*-spacing values from XRD patterns (Fig. 3). Vibration bands below 700 cm^{-1} correspond to M–O–M modes, with a band near 400 cm^{-1} indicating Ni- or Mg–Al octahedral coordination (M–O_6). The hybrid solids show Fe–O vibrations at 628 and 580 cm^{-1}, confirming the presence of M7 in the core@shell structures. These bands are more intense than those from the LDH, reflecting the higher proportion of magnetite relative to the layered solid.[44,46,47]

3.3 Synthesis of metalloporphyrin (MP), preparation of M7@LDH@MP solid and catalytic evaluation

3.3.1 Characterization of free-base porphyrin and MP. The free-base neutral porphyrin [H_2(TDFPP)] and the tetra-anionic free-base porphyrin Na_4[H_2(TDFSPP)] (H_2P) ligands were previously characterized through ^{1}H NMR, FTIR, UV-VIS techniques[13] confirming their preparation.

The characterization of the complexes resulting from the tetra-anionic free-base porphyrin Na_4[H_2(TDFSPP)] (H_2P) metalation with manganese(III) – Na_4[Mn(TDFSPP)(Oac)], iron(III) – Na_4[Fe(TDFSPP)]Cl, zinc(II) – Na_4[Zn(TDFSPP)] and magnesium(II) – Na_4[Mg(TDFSPP)], or simply MnP, FeP, ZnP and MgP, respectively, was made by UV-VIS spectroscopy (Fig. 7A).

The UV-VIS spectrum of H_2P (Fig. 7A, black line) shows the characteristic electronic-transition Soret band, the most intense peak of the porphyrin structure, at 407 nm, along with four Q bands between 500 and 650 nm, corresponding to vibrational transitions.[6,89,90] Upon complexation with metal ions (Fe^{3+}, Zn^{2+}, Mn^{3+}, and Mg^{2+}), leading to Soret band shifts to specific wavelengths: 388 nm for FeP,[91] 417 nm for ZnP,[92] 460 nm for MnP,[93] and 423 nm for MgP[94] (Fig. 7A, brown, orange, red, and pink lines, respectively) due to symmetry changes induced by metal insertion. Additionally, this change reduces the number of Q bands from four to two in the 500–650 nm region. For MnP (Fig. 7, red line), distinct charge transfer bands at 328, 372, and 394 nm are also observed, typical of manganese–porphyrin complexes (hyperporphyrin).[6,95]

The FTIR spectra of the free base porphyrin (H_2P) and metalloporphyrins (FeP, MnP, ZnP, and MgP) are shown in Fig. 7B. The spectrum of the free base porphyrin Na_4[H_2(TDFSPP)] has been previously discussed.[13] A key feature for MP characterization *via* FTIR is the absence of the N–H angular vibration band around 1600 cm^{-1}, indicating nitrogen deprotonation upon metal ion insertion into the porphyrin ring.[74]

The FTIR spectrum of MnP provides additional insights into the nature of the axial ligand interaction (covalent or charge compensation). The bands associated with the asymmetric and symmetric deformation of the acetate group (O–C=O) appear in the ranges 1578–1414 cm^{-1} (Δ = 164 cm^{-1}) and 1539–1382 cm^{-1} (Δ = 157 cm^{-1}), confirming acetate as the counterion.[15,74] For FeP, the band corresponding to the interaction

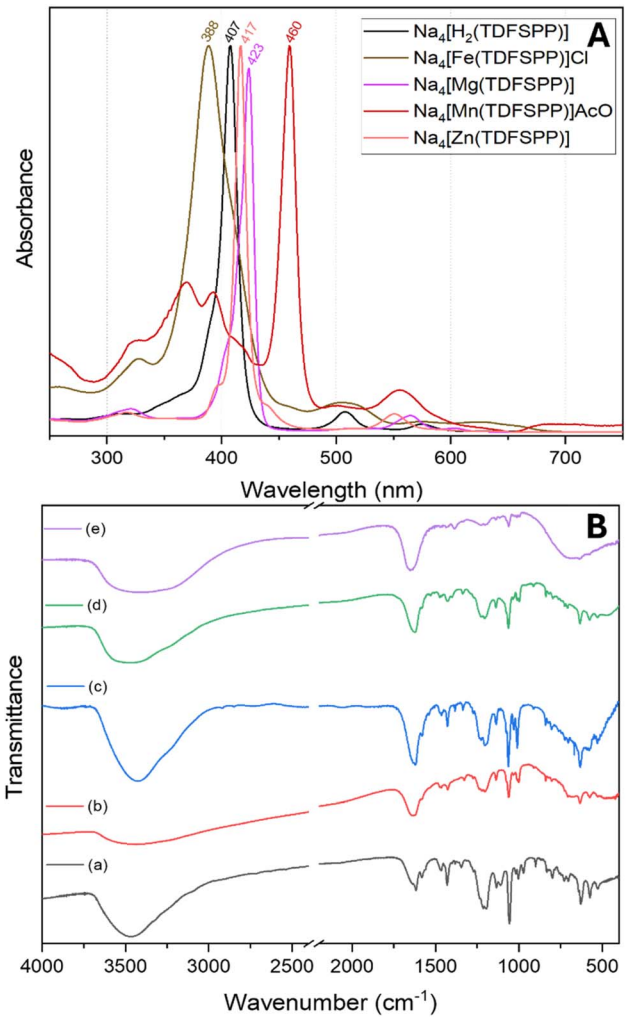

Fig. 7 (A) UV-VIS spectra of the (a) tetra-anionic free-base porphyrin H2P ligand, (b) FeP, (c) MgP, (d) MnP and (e) ZnP complexes in ethanolic solution. (B) FTIR spectra of the free-base porphyrin (a) Na_4[H_2(TDFSPP)] (H_2P), and the metalloporphyrins (b) iron(III) porphyrin complex Na_4[Fe(TDFSPP)]Cl (FeP) (c) manganese(III)porphyrin complex Na_4[Mn(TDFSPP)Oac] (MnP), (d) zinc(II) porphyrin complex Na_4[Zn(TDFSPP)] (ZnP) and (e) magnesium(II) porphyrin complex Na_4[Mg(TDFSPP)] (MgP) in the 400–4000 cm^{-1} region.

with chloride ions is expected near 360 cm^{-1}, but it is beyond the spectral range of the recorded FTIR spectrum.

3.3.2 Preparation and characterization of core@shell/MP. The immobilization of tetra-anionic metalloporphyrins MPs (FeP, MnP, ZnP, and MgP) onto the core@shell solids occurs through electrostatic interactions with residual positive charges on the MA or NA-LDH shell.[13,93,96] The immobilization loading was quantified *via* UV-VIS analysis of the supernatant, based on the MP concentration (Table 4).[13,16,96]

The loading values align with those reported for electrostatic interactions with other supports.[13,14,58,80,93] High loading efficiency reflects the low MP amount used and the high positive charge density on the LDH layers, resulting from the synthesis method, which provided high surface area and mesoporosity. This also facilitated MP trapping within the slit-like pores.[13,14,93]

Table 4 Loading values and immobilization percentages of the MnP on the prepared supports

	Immobilization degree (%)[a]/loading (mol g^{-1})[b]			
Solid	MnP	FeP	ZnP	MgP
M7@MA-6@MP	99/1.12 × 10^{-5}	100/1.05 × 10^{-5}	100/1.04 × 10^{-5}	96/9.56 × 10^{-6}
M7@NA-4@MP	99/9.223 × 10^{-6}	100/1.12 × 10^{-5}	100/1.06 × 10^{-5}	98/1.02 × 10^{-5}

[a] Immobilization degree = (mol of MP immobilized on the support/mol of MP used in the immobilization process) × 100. [b] Loading value: amount (mol) of MP immobilized per g of core@shell support.

As tetra-anionic MPs require positive charge for immobilization, M7 was not tested, as it holds negative charges instead.

The FTIR spectra for M7@MA-0.6 and M7@NA-0.4 solids containing FeP, MnP, ZnP, or MgP do not indicate the presence of MPs due to the low amount used for immobilization, with only the core@shell bands being visible (Fig. SI 8).[13,97,98]

Similarly, the XRD patterns show no difference between the solid supports and the MP-loaded solids (Fig. SI 9). This is attributed to surface interactions on the MA or NA-LDH shell rather than intercalation within the layers, which would not affect the diffraction pattern.[99]

3.3.3 Catalytic investigation of the M@LDH@MP in cyclooctene oxidation. The prepared solids (M7@MA-6@FeP, M7@MA-6@MnP, M7@MA-6@MgP, M7@MA-6@ZnP, M7@NA-4@FeP, M7@NA-4@MnP, M7@NA-4@MgP, and M7@NA-4@ZnP) were tested as catalysts in the cyclooctene oxidation reaction, a diagnostic test for evaluating the catalytic potential of MPs in oxidation processes.[12,100] Using iodosylbenzene (PhIO) as the oxidant, the reaction selectively yielded *cis*-cyclooctene oxide as the sole product.[5,13,101,102] The experiments were conducted under the following conditions: MP/PhIO/cyclooctene molar ratio of 1 : 20 : 2000, room temperature, 1 hour reaction time, in acetonitrile and magnetic stirring. The results are summarized in Table 5.

Table 5 Cyclooctene oxidation with PhIO[a] as oxidant catalyzed by the different catalysts prepared in this work and control reactions (blank)

Entry	Catalyst	Cyclooctene oxide yield (%)[b]
1	None	2.4 ± 0.4
2	M7	20.2 ± 6.3
3	MA-LDH	29.0 ± 0.9
4	NA-LDH	15.8 ± 1.2
5	M7@MA-6	1.7 ± 0.2
6	M7@NA-4	3.4 ± 0.3
7	FeP[3]	87.4 ± 8.0
8	MnP[c]	40.4 ± 1.2
9	ZnP[c]	43.6 ± 7.4
10	MgP[c]	22.6 ± 1.8
11	M7@MA-6@FeP	80.0 ± 1.3
12	M7@MA-6@MnP	81.9 ± 0.01
13	M7@MA-6@ZnP	19.1 ± 0.6
14	M7@MA-6@MgP	1.9 ± 0.2
15	M7@NA-4@FeP	67.1 ± 2.1
16	M7@NA-4@MnP	74.7 ± 0.02
17	M7@NA-4@ZnP	7.1 ± 0.8
18	M7@NA-4@MgP	2.1 ± 0.2

[a] Reaction conditions: MnP/PhIO/cyclooctene molar ratio of 1 : 20 : 2000, under argon atmosphere and magnetic stirring, absence of light, for 1 h. [b] Yield based on PhIO. [c] Homogeneous catalysis.

The control reactions results are presented in entries number 1 to 6 (Table 5). The reaction without a catalyst (Table 5, entry 1) yielded very low product under the catalytic reaction conditions investigated. However, using the different solid supports prepared (entries 2–4) they were observed some unexpected epoxide yield, likely due to radical oxidation pathways involving PhIO$^{\bullet}$ species or intermediate PhIO–M–OH complexes at surface solid sites.[13,100,103,104]

In contrast, the core@shell solids (entries 5 and 6) exhibited a 15-fold reduction in yield, suggesting that the interaction between the core and shell blocked or deactivated the sites on magnetite and on LDHs, to act as catalyst in this reaction, as reported in the literature.[105]

The catalytic performance differences between the MPs are associated with the distinct ability of the central metal ions to access high-valent metal–oxo intermediates.[5,13,15,90,101,103,106–108] For iron(III) and Manganese(III) porphyrins, one-electron oxidation of the metal center and concomitant porphyrin π-radical delocalization generate the reactive Fe(IV)=O or Mn(V)=O species—analogous to Compound I in cytochrome P450—which mediate efficient oxygen atom transfer to cyclooctene. In contrast, Zn(II) and Mg(II) porphyrins are redox-inert and cannot undergo metal-centered oxidation; thus, catalytic turnover depends solely on outer-sphere activation of PhIO through weak π–π or hydrogen-bonding interactions with the macrocycle.[108]

In homogeneous catalysis (entries 7–10), FeP provided the highest yield (entry 7), as expected from its ability to form high-valent intermediates.[5,13,15,103,106,107] MnP (entry 8) showed lower yields probably due to its reduced solubility in acetonitrile, which limited reactant interaction.[5,11] The moderate yields

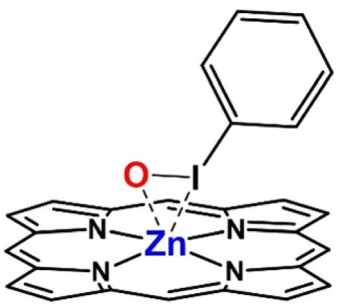

Fig. 8 Representative intermediary PhIO–Zn complex that would favor the oxygen transfer to substrate.

observed for ZnP and MgP (entries 9 and 10) suggest an alternative mechanism for both, however more efficient for ZnP, potentially involving direct olefin interaction with a hypervalent iodine complex, as reported by Nam and co-workers using PhIO as the oxidant (Fig. 8).[108]

Entries 11–18 (Table 5) show the yield of *cis*-cyclooctene oxide for the immobilized complexes on core@shell solids (heterogeneous catalysis). In general, a higher yield trend is observed using as support to the MP the solid with the MA-LDH (entries 11 to 14) compared to the solid with the NA-LDH (entries 15 to 18) suggesting a better MP arrangement of the support Mg_3Al LDH-based core@shell (M7@MA-6), resulted by the differences in core–shell interaction and textural properties of this solid in comparison to the solid with Ni_3Al-LDH (M7@NA-4), causing a better diffusion of the reactants to the active MP center and increase the catalytic yield.[58]

MP-based catalysts (entries 11 to 18), showed lower yields than in homogeneous catalysis (entry 7 to 10), as expected for immobilized catalysts (heterogeneous catalysis) in comparison to the homogeneous ones, due to reduced diffusion.[15,109] In contrast, MnP catalysts (entries 12 and 16) outperformed their homogeneous counterparts (entry 8), likely because immobilization mitigated MnP's poor solubility in acetonitrile.[13] The results confirm that the MPs remain the primary active catalysts in the heterogeneous systems.

The immobilized ZnP and MgP catalysts (entries 13, 14, 17 and 18) exhibited the lower yields compared to immobilized MnP and FeP and their homogeneous counterparts (entries 9, 10), suggesting that immobilization of both may hinder the formation of oxidation intermediates relevant in the catalytic activity (Fig. 8). Additionally, interactions between Zn or Mg and oxygen species on the solid surface may inhibit the oxidation mechanism for these to metalloporphyrins.

Catalyst stability and reusability were evaluated for M7@MA-6 and M7@NA-4 containing FeP and MnP (Table 6). In general, for all the 4 solids investigated after the first use about 30–40% yield drop was observed (*e.g.*, Table 6, entry 1 *vs.* entry 2, drop of the cyclooctenoxide yield = 43%), likely due to some leaching of the MP-layered shell during recovery and washing with acetonitrile.[14,78,103] However, the stabilization of yield in the subsequent cycles was observed (*e.g.*, entries 3–6) suggests that further leaching was minimized. Another interesting observation in the results present on Table 6 is that the MP immobilized on the solid support M7@NA presented the smallest drop in yield values when comparing the first and second use of the catalysts (*e.g.* entries 7 and 8, drop of the cyclooctenoxide yield = 33% in comparison to entries 1 and 2, drop of the cyclooctenoxide yield = 43%). These results suggesting that the arrangement of the HDL layer on the magnetic particle favored better immobilization of the metalloporphyrins on the support, becoming the more stable catalyst for recycling. These differences likely arise from the distinct interactions and morphologies of MA- and NA-LDH on magnetite. MA-LDH interacts electrostatically with the core, leading to easier detachment, while NA-LDH can form covalent bonds, making the NA-based catalysts more stable across reuse cycles. Although both Mg_3Al-LDH (MA) and Ni_3Al-LDH (NA) coatings were synthesized under identical solvothermal core@shell conditions, their interfacial behavior toward magnetite can differ due to intrinsic electronic and structural properties of the divalent cations. Ni^{2+} possesses a partially filled $3d^8$ configuration capable of establishing covalent (Ni–O–Fe) linkages at the interface through orbital overlap with surface Fe 3d and O 2p orbitals. In contrast, Mg^{2+}, with a closed-shell configuration and more ionic bonding character, interacts predominantly through electrostatic attraction between the positively charged LDH layers and the negatively charged magnetite surface.[42,44,46–50,69,84,87]

Table 6 Reuse of core@shell catalysts containing FeP or MnP in cyclooctene oxidation[a]

Entry	Catalyst	Cyclooctenoxide/ yield (%)[b]	Drop (−) of the yield
1	M7@MA-6@FeP	80.0 ± 1.3	−43%
2	1° reuse	45.6 ± 3.1	
3	2° reuse	48.5 ± 1.4	
4	3° reuse	49.0 ± 0.8	
5	4° reuse	43.0 ± 2.0	
6	5° reuse	45.6 ± 0.5	
7	M7@NA-4@FeP	67.1 ± 2.1	−33%
8	1° reuse	45.6 ± 2.5	
9	2° reuse	49.5 ± 2.3	
10	3° reuse	42.2 ± 3.0	
11	4° reuse	40.5 ± 2.4	
12	5° reuse	39.2 ± 2.6	
13	M7@MA-6@MnP	81.9 ± 0.01	−42%
14	1° reuse	48.3 ± 1.2	
15	2° reuse	56.9 ± 0.1	
16	3° reuse	53.8 ± 3.2	
17	4° reuse	42.2 ± 0.04	
18	5° reuse	43.7 ± 1.3	
19	M7@NA-4@MnP	74.7 ± 0.02	−27%
20	1° reuse	54.4 ± 0.1	
21	2° reuse	50.9 ± 0.7	
22	3° reuse	50.7 ± 1.0	
23	4° reuse	44.1 ± 0.1	
24	5° reuse	52.7 ± 2.7	

[a] Reaction conditions: MnP/PhIO/cyclooctene molar ratio of 1 : 20 : 2000, under argon atmosphere and magnetic stirring, absence of light, for 1 h. [b] Yield based on PhIO.

The consistent performance across reuse cycles indicates that the catalysts stabilize on the support and remain suitable for recycling.

SEM images after the fifth reuse (Fig. SI 10) suggest that M7@MA@FeP shows loss of layered material (Fig. SI 10A) in comparison to M7@NA@FeP (Fig. SI 10B), although with low resolution/focus due to the challenges associated with the material's nature. This could imply fewer metalloporphyrins in M7@MA@FeP, contributing to decreased catalytic efficiency after the reuse. The recycling experiments pointed that it was critical after the first use, stabilizing for the subsequent reuses. The electrostatic interaction between magnesium LDH and magnetite makes it more prone to detachment, leading to MP loss and reduced yield. In contrast, the covalent interaction between nickel LDH and magnetite results in more robust catalysts, with only ~30% yield reduction compared to ~40% for M7@MA@MP after reuse.

4 Conclusion

We successfully report a well-structured and reproducible method of core@shell support preparation composed of about 200 nm magnetite (Fe_3O_4) and a shell of Mg_3Al or Ni_3Al LDH. The iron(III), manganese(III), zinc(II), or magnesium(II) porphyrins MP-containing solids were designed for easy recovery and multicatalytic functionality.

Magnetite was synthesized *via* a microwave-assisted solvothermal route, with optimized LDH coverage ensuring proper core@shell formation. Eight MP-containing solids were evaluated in cyclooctene epoxidation using PhIO as an oxidant in where FeP and MnP showed the best catalytic performance, with MnP excelling post-immobilization and easy reusability keeping the catalytic performance for at least 5 recycling experiments.

Future studies will explore these catalysts in diverse single and sequential reactions to assess their multicatalytic potential.

Author contributions

Everton Henrique dos Santos: conceptualization, methodology, investigation, writing – original draft. Adriana Duarte Dalla Costa: methodology, investigation, writing – original draft. Vanessa Prevot: formal analysis, data curation, validation, writing – review & editing. Claude Forano: formal analysis, funding acquisition, writing – review & editing. Shirley Nakagaki: conceptualization, supervision, project administration, funding acquisition, writing – review & editing.

Conflicts of interest

There are no conflicts to declare.

Data availability

The data that support the findings of this study are available from the corresponding author upon reasonable request.

Supplementary information (SI) is available. See DOI: https://doi.org/10.1039/d5ra08288a.

Acknowledgements

The authors are grateful to Coordenação de Aperfeiçoamento de Pessoal de Nível Superior (CAPES – Finance code 001 and CAPES- PrInt/PROCESSO 88881.311981/2018–01), Conselho Nacional de Desenvolvimento Científico e Tecnológico (CNPq: SN projects – 301876/2019–3 and 405217/2018–8;), Instituto Nacional de Ciência e Tecnologia em Ciências moleculares (INCT-CIMOL Projeto CNPq 406804/2022-2), Fundação Araucária and Centro de Microscopia da UFPR (CME/UFPR).

References

1 J. Han, H. Gong, X. Ren and X. Yan, Supramolecular nanozymes based on peptide self-assembly for biomimetic catalysis, *Nano Today*, 2021, **41**, 101295–101313, DOI: 10.1016/j.nantod.2021.101295.

2 G. Lan, Y. Fan, W. Shi, E. You, S. S. Veroneau and W. Lin, Biomimetic active sites on monolayered metal–organic frameworks for artificial photosynthesis, *Nat. Catal.*, 2022, **5**, 1006–1018, DOI: 10.1038/s41929-022-00865-5.

3 D. Mansuy, A brief history of the contribution of metalloporphyrin models to cytochrome P450 chemistry and oxidation catalysis, *Comptes Rendus. Chim.*, 2007, **10**, 392–413, DOI: 10.1016/j.crci.2006.11.001.

4 T. Omura and R. Sato, A New Cytochrome in Liver Microsomes, *J. Biol. Chem.*, 1962, **237**, PC1375–PC1376, DOI: 10.1016/S0021-9258(18)60338-2.

5 B. Meunier, Metalloporphyrins as versatile catalysts for oxidation reactions and oxidative DNA cleavage, *Chem. Rev.*, 1992, **92**, 1411–1456, DOI: 10.1021/cr00014a008.

6 D. Dolphin, T. G. Traylor and L. Y. Xie, Polyhaloporphyrins: Unusual Ligands for Metals and Metal-Catalyzed Oxidations, *Acc. Chem. Res.*, 1997, **30**, 251–259, DOI: 10.1021/ar960126u.

7 P. Zardi, D. Intrieri, A. Caselli and E. Gallo, Co(porphyrin)-catalysed amination of 1,2-dihydronaphthalene derivatives by aryl azides, *J. Organomet. Chem.*, 2012, **716**, 269–274, DOI: 10.1016/j.jorganchem.2012.07.013.

8 T. Ema, Y. Miyazaki, J. Shimonishi, C. Maeda and J. Hasegawa, Bifunctional Porphyrin Catalysts for the Synthesis of Cyclic Carbonates from Epoxides and CO 2 : Structural Optimization and Mechanistic Study, *J. Am. Chem. Soc.*, 2014, **136**, 15270–15279, DOI: 10.1021/ja507665a.

9 G. Ramírez, G. Ferraudi, Y.-Y. Chen, E. Trollund and D. Villagra, Enhanced photoelectrochemical catalysis of CO2 reduction mediated by a supramolecular electrode of packed CoII(tetrabenzoporphyrin), *Inorg. Chim. Acta*, 2009, **362**, 5–10, DOI: 10.1016/j.ica.2007.08.024.

10 E. H. Santos, C. Carvalho, C. M. Terzi and S. Nakagaki, Recent Advances in Catalyzed Sequential Reactions and the Potential Use of Tetrapyrrolic Macrocycles as Catalysts, *Molecules*, 2018, **23**, 2796–2815, DOI: 10.3390/molecules23112796.

11 Y. Iamamoto, M. D. Assis, K. J. Ciuffi, H. C. Sacco, L. Iwamoto, A. J. B. Melo, O. R. Nascimento and C. M. C. Prado, Factors which affect the catalytic activity of iron(III) meso tetrakis(2,6-dichlorophenyl) porphyrin chloride in homogeneous system, *J. Mol. Catal. A: Chem.*, 1996, **109**, 189–200, DOI: 10.1016/1381-1169(96)00030-1.

12 G. M. Ucoski, F. S. Nunes, G. DeFreitas-Silva, Y. M. Idemori and S. Nakagaki, Metalloporphyrins immobilized on silica-coated Fe3O4 nanoparticles: Magnetically recoverable catalysts for the oxidation of organic substrates, *Appl. Catal., A*, 2013, **459**, 121–130, DOI: 10.1016/j.apcata.2013.03.012.

13 R. M. da Silva Junior, E. H. dos Santos and S. Nakagaki, Metalloporphyrin-based multifunctional catalysts for one-pot assisted Tandem reaction, *Mol. Catal.*, 2023, **541**, 113080–113097, DOI: 10.1016/j.mcat.2023.113080.

14 G. S. Machado, G. G. C. Arízaga, F. Wypych and S. Nakagaki, Immobilization of anionic metalloporphyrins on zinc hydroxide nitrate and study of an unusual catalytic activity, *J. Catal.*, 2010, **274**, 130–141, DOI: 10.1016/j.jcat.2010.06.012.

15 K. C. M. Westrup, R. M. da Silva Junior, K. M. Mantovani, L. Bach, J. F. Stival, P. G. P. Zamora, F. Wypych, G. S. Machado and S. Nakagaki, Light-assisted cyclohexane oxidation catalysis by a manganese(III) porphyrin immobilized onto zinc hydroxide salt and zinc oxide obtained by zinc hydroxide salt hydrothermal decomposition, *Appl. Catal., A*, 2020, **602**, 117708–117720, DOI: 10.1016/j.apcata.2020.117708.

16 G. M. Ucoski, V. H. A. Pinto, G. DeFreitas-Silva, J. S. Rebouças, R. M. da Silva Junior, I. Mazzaro, F. S. Nunes and S. Nakagaki, Manganese porphyrins immobilized on magnetic SBA-15 mesoporous silica as selective and efficient catalysts for cyclic and linear alkane oxidation, *Microporous Mesoporous Mater.*, 2018, **265**, 84–97, DOI: 10.1016/j.micromeso.2018.02.003.

17 J. F. Stival, S. L. A. Marin, P. G. P. Zamora, J. S. Rebouças, F. Gröhn, S. Bernhardt, F. Wypych and S. Nakagaki, Metalloporphyrin/ZnO solids as selective catalysts for oxidation reaction assisted by light, *Appl. Catal., A*, 2023, **662**, 119271–119283, DOI: 10.1016/j.apcata.2023.119271.

18 J. Meng, Y. Zhao, H. Li, R. Chen, X. Sun and X. Sun, Metalloporphyrin immobilized CeO 2 : in situ generation of active sites and synergistic promotion of photocatalytic water oxidation, *Catal. Sci. Technol.*, 2021, **11**, 2560–2569, DOI: 10.1039/D0CY02409K.

19 F. Zhang, Y. Xie, P. Liu, F. Hao, Z. Yao and H. Luo, Cycloaddition Reaction of Propylene Oxide and Carbon Dioxide Over NaX Zeolite Supported Metalloporphyrin Catalysts, *Catal. Lett.*, 2014, **144**, 1894–1899, DOI: 10.1007/s10562-014-1360-z.

20 F. Rafiee, H. Hassani Ardeshiri, A. Gholami, H. Ghafuri and R. Rahimi, Synthesis and characterization of new photocatalyst-based tin (IV) 5, 10, 15, 20-tetrakis (4-benzhydryl benzoate) porphyrin immobilized on Fe3O4 nanoparticles for removal of organic dye from wastewater, *Mater. Sci. Eng., B*, 2024, **308**, 117574–117588, DOI: 10.1016/j.mseb.2024.117574.

21 X. Zhou and H. Ji, Cobalt Porphyrin Immobilized on Montmorillonite: A Highly Efficient and Reusable Catalyst for Aerobic Oxidation of Alcohols to Carbonyl Compounds, *Chin. J. Catal.*, 2012, **33**, 1906–1912, DOI: 10.1016/S1872-2067(11)60461-0.

22 Z. Li, C. Wang, Z. Su, W. Zhang, N. Wang, G. Mele and J. Li, New porphyrin/Cu(II) porphyrin-TiO2 nanohybrids for improved photocatalytic oxidation and reduction activities, *Mater. Chem. Phys.*, 2020, **252**, 123228–123241, DOI: 10.1016/j.matchemphys.2020.123228.

23 C. Shen, L. Liu, J. Ma, J. Zhou, S. Zhang, H. Cheng, Y. Ge, T. Zhang, Z. Tong and B. Zhang, The direct assembly of metalloporphyrin and Mg–Al layered double hydroxides nanosheets: a highly efficient catalyst for the green epoxidation of olefins, *J. Mater. Sci.*, 2020, **55**, 11714–11726, DOI: 10.1007/s10853-020-04737-w.

24 Z. Zhang and S. Satpathy, Electron states, magnetism, and the Verwey transition in magnetite, *Phys. Rev. B:Condens. Matter Mater. Phys.*, 1991, **44**, 13319–13331, DOI: 10.1103/PhysRevB.44.13319.

25 F. Hassanzadeg-Afruzi, Z. Amiri-Khamakani, M. Saeidirad, M. M. Salehi, R. Taheri-Ledari and A. Maleki, Facile synthesis of pyrazolopyridine pharmaceuticals under mild conditions using an algin-functionalized silica-based magnetic nanocatalyst (Alg@SBA-15/Fe3O4), *RSC Adv.*, 2023, **15**, 10367–10378, DOI: 10.1039/D2RA07228A.

26 M. Kosmulski, Isoelectric points and points of zero charge of metal (hydr)oxides: 50years after Parks' review, *Adv. Colloid Interface Sci.*, 2016, **238**, 1–61, DOI: 10.1016/j.cis.2016.10.005.

27 H. S. S. Panda and D. Bahadur, Study of the preparation, properties and kinetics of anion release in drug intercalated magnetic nanohybrids, *Mater. Res. Bull.*, 2012, **47**, 571–579, DOI: 10.1016/j.materresbull.2011.12.041.

28 Y. Li, H.-Y. Y. Bi, H. Li, X.-M. M. Mao and Y.-Q. Q. Liang, Synthesis, characterization, and sustained release property of Fe 3 O 4 @(enrofloxacin-layered double hydroxides) nanocomposite, *Mater. Sci. Eng., C*, 2017, **78**, 886–891, DOI: 10.1016/j.msec.2017.04.104.

29 C. Salazar-Camacho, M. Villalobos, M. d. l. L. Rivas-Sánchez, J. Arenas-Alatorre, J. Alcaraz-Cienfuegos and M. E. Gutiérrez-Ruiz, Characterization and surface reactivity of natural and synthetic magnetites, *Chem. Geol.*, 2013, **347**, 233–245, DOI: 10.1016/j.chemgeo.2013.03.017.

30 D. Santos-Carballal, A. Roldan, R. Grau-Crespo and N. H. de Leeuw, A DFT study of the structures, stabilities and redox behaviour of the major surfaces of magnetite Fe 3 O 4, *Phys. Chem. Chem. Phys.*, 2014, **16**, 21082–21097, DOI: 10.1039/C4CP00529E.

31 A. S. Katheras, K. Karalis, M. Krack, A. C. Scheinost and S. V. Churakov, Stability and Speciation of Hydrated Magnetite {111} Surfaces from Ab Initio Simulations with Relevance for Geochemical Redox Processes, *Environ. Sci. Technol.*, 2024, **58**, 935–946, DOI: 10.1021/acs.est.3c07202.

32 D. Zhang, C. Lu, Y. Ni, Z. Xu and W. Zhang, Effect of water on size-controllable synthesis of mesoporous Fe3O4 microspheres and their applications in waste water treatment, *CrystEngComm*, 2013, **15**, 4755–4764, DOI: 10.1039/c3ce26971j.

33 A. P. Philipse, M. P. B. Van Bruggen and C. Pathmamanoharan, Magnetic Silica Dispersions: Preparation and Stability of Surface-Modified Silica Particles with a Magnetic Core, *Langmuir*, 1994, **10**, 92–99, DOI: 10.1021/la00013a014.

34 S. V. Salihov, Y. A. Ivanenkov, S. P. Krechetov, M. S. Veselov, N. V. Sviridenkova, A. G. Savchenko, N. L. Klyachko, Y. I. Golovin, N. V. Chufarova, E. K. Beloglazkina and A. G. Majouga, Recent advances in the synthesis of Fe3O4@AU core/shell nanoparticles, *J. Magn. Magn.*

Mater., 2015, **394**, 173–178, DOI: 10.1016/j.jmmm.2015.06.012.

35 S. B. Atla, W.-R. Lin, T.-C. Chien, M.-J. Tseng, J.-C. Shu, C.-C. Chen and C.-Y. Chen, Fabrication of Fe3O4/ZnO magnetite core shell and its application in photocatalysis using sunlight, *Mater. Chem. Phys.*, 2018, **216**, 380–386, DOI: 10.1016/j.matchemphys.2018.06.020.

36 V. E. Noval and J. G. Carriazo, Fe3O4-TiO2 and Fe3O4-SiO2 Core-shell Powders Synthesized from Industrially Processed Magnetite (Fe3O4) Microparticles, *Mater. Res.*, 2019, **22**(3), e20180660, DOI: 10.1590/1980-5373-mr-2018-0660.

37 M. S. A. Darwish, U. Peuker, U. Kunz and T. Turek, Bi-layered polymer–magnetite core/shell particles: synthesis and characterization, *J. Mater. Sci.*, 2011, **46**, 2123–2134, DOI: 10.1007/s10853-010-5048-5.

38 S. Nakagaki, G. S. Machado, J. F. Stival, E. H. Santos, G. M. Silva and F. Wypych, Natural and synthetic layered hydroxide salts (LHS): Recent advances and application perspectives emphasizing catalysis, *Prog. Solid State Chem.*, 2021, **64**, 100335, DOI: 10.1016/j.progsolidstchem.2021.100335.

39 R. Sharma, G. G. C. Arízaga, A. K. Saini and P. Shandilya, Layered double hydroxide as multifunctional materials for environmental remediation: from chemical pollutants to microorganisms, *Sustain. Mater. Technol.*, 2021, **29**, e00319, DOI: 10.1016/j.susmat.2021.e00319.

40 S. He, Z. An, M. Wei, D. G. Evans and X. Duan, Layered double hydroxide-based catalysts: nanostructure design and catalytic performance, *Chem. Commun.*, 2013, **49**, 5912, DOI: 10.1039/c3cc42137f.

41 I.-K. K. Jung, Y. Jo, S.-C. C. Han and J.-I. Il Yun, Efficient removal of iodide anion from aqueous solution with recyclable core-shell magnetic Fe3O4@Mg/Al layered double hydroxide (LDH), *Sci. Total Environ.*, 2020, **705**, 135814, DOI: 10.1016/j.scitotenv.2019.135814.

42 Z. Lin and J. Chen, Magnetic Fe3O4@MgAl-LDH@La(OH)3 composites with a hierarchical core-shell structure for phosphate removal from wastewater and inhibition of labile sedimentary phosphorus release, *Chemosphere*, 2021, **264**, 128551–128561, DOI: 10.1016/j.chemosphere.2020.128551.

43 X. Zhang, B. Hu, Y. Zhao, Y. Yang, Z. Gao, K. Nishinari, J. Yang, Y. Zhang and Y. Fang, Electrostatic Interaction-Based Fabrication of Calcium Alginate–Zein Core–Shell Microcapsules of Regulable Shapes and Sizes, *Langmuir*, 2021, **37**, 10424–10432, DOI: 10.1021/acs.langmuir.1c01098.

44 X. Gao, L. Niu, X. Qiao, W. Feng, Y. Cao and G. Bai, Facile Preparation of a Stable Fe3O4@LDH@NiB Magnetic Core-Shell Nanocomposite for Hydrogenation, *Chin. J. Chem.*, 2017, **35**, 1149–1156, DOI: 10.1002/cjoc.201600759.

45 R. Hayes, A. Ahmed, T. Edge and H. Zhang, Core–shell particles: Preparation, fundamentals and applications in high performance liquid chromatography, *J. Chromatogr., A*, 2014, **1357**, 36–52, DOI: 10.1016/j.chroma.2014.05.010.

46 P. Kumar, K. Gill, S. Kumar, S. K. Ganguly and S. L. Jain, Magnetic Fe3O4@MgAl–LDH composite grafted with cobalt phthalocyanine as an efficient heterogeneous catalyst for the oxidation of mercaptans, *J. Mol. Catal. A: Chem.*, 2015, **401**, 48–54, DOI: 10.1016/j.molcata.2015.03.001.

47 X. Chen, F. Mi, H. H. Zhang and H. H. Zhang, Facile synthesis of a novel magnetic core-shell hierarchical composite submicrospheres Fe3O4@CuNiAl-LDH under ambient conditions, *Mater. Lett.*, 2012, **69**, 48–51, DOI: 10.1016/j.matlet.2011.11.052.

48 R. G. L. Gonçalves, P. A. Lopes, J. A. Resende, F. G. Pinto, J. Tronto, M. C. Guerreiro, L. C. A. de Oliveira, W. de Castro Nunes and J. L. Neto, Performance of magnetite/layered double hydroxide composite for dye removal via adsorption, Fenton and photo-Fenton processes, *Appl. Clay Sci.*, 2019, **179**, 105152–105161, DOI: 10.1016/j.clay.2019.105152.

49 V. Yousefi, V. Tarhriz, S. Eyvazi and A. Dilmaghani, Synthesis and application of magnetic@layered double hydroxide as an anti-inflammatory drugs nanocarrier, *J. Nanobiotechnology.*, 2020, **18**, 155–165, DOI: 10.1186/s12951-020-00718-y.

50 S. Yin, J. Li and H. Zhang, Hierarchical hollow nanostructured core@shell recyclable catalysts γ-Fe2O3 @LDH@Au 25 -x for highly efficient alcohol oxidation, *Green Chem.*, 2016, **18**, 5900–5914, DOI: 10.1039/C6GC01290F.

51 J. G. Sharefkin and H. Saltzman, Iodosobenzene Diacetate, *Org. Synth.*, 1963, **43**, 62, DOI: 10.15227/orgsyn.043.0062.

52 B. J. Littler, Y. Ciringh and J. S. Lindsey, Investigation of Conditions Giving Minimal Scrambling in the Synthesis of trans -Porphyrins from Dipyrromethanes and Aldehydes, *J. Org. Chem.*, 1999, **64**, 2864–2872, DOI: 10.1021/jo982452o.

53 H. Turk and W. T. Ford, Epoxidation of styrene with aqueous hypochlorite catalyzed by a manganese(III) porphyrin bound to colloidal anion-exchange particles, *J. Org. Chem.*, 1991, **56**, 1253–1260, DOI: 10.1021/jo00003a058.

54 P. Rothemund and A. Menotti, Porphyrin Studies. V. The Metal Complex Salts of TPP, *J. Am. Chem. Soc.*, 1948, **70**, 1808–1812.

55 A. D. Adler, F. R. Longo, F. Kampas and J. Kim, On the preparation of metalloporphyrins, *J. Inorg. Nucl. Chem.*, 1970, **32**, 2443–2445, DOI: 10.1016/0022-1902(70)80535-8.

56 H. Deng, X. Li, Q. Peng, X. Wang, J. Chen and Y. Li, Monodisperse Magnetic Single-Crystal Ferrite Microspheres, *Angew. Chem., Int. Ed.*, 2005, **44**, 2782–2785, DOI: 10.1002/anie.200462551.

57 J. Inacio, C. Taviot-Guého, C. Forano and J. Besse, Adsorption of MCPA pesticide by MgAl-layered double hydroxides, *Appl. Clay Sci.*, 2001, **18**, 255–264, DOI: 10.1016/S0169-1317(01)00029-1.

58 S. Nakagaki, K. Mantovani, G. S. Machado, K. D. F. Castro and F. Wypych, Recent Advances in Solid Catalysts Obtained by Metalloporphyrins Immobilization on

Layered Anionic Exchangers: A Short Review and Some New Catalytic Results, *Molecules*, 2016, **21**, 291–315, DOI: 10.3390/molecules21030291.

59 G. Zanchettin, G. da S. Falk, S. Y. G. González and D. Hotza, High performance magnetically recoverable Fe3O4 nanocatalysts: fast microwave synthesis and photo-fenton catalysis under visible-light, *Chem. Eng. Process. Process Intensif.*, 2021, **166**, 108438–108445, DOI: 10.1016/j.cep.2021.108438.

60 E. M. Kostyukhin and L. M. Kustov, Microwave-assisted synthesis of magnetite nanoparticles possessing superior magnetic properties, *Mendeleev Commun.*, 2018, **28**, 559–561, DOI: 10.1016/j.mencom.2018.09.038.

61 A. A. Hernández-Hernández, G. A. Álvarez-Romero, A. Castañeda-Ovando, Y. Mendoza-Tolentino, E. Contreras-López, C. A. Galán-Vidal and M. E. Páez-Hernández, Optimization of microwave-solvothermal synthesis of Fe3O4 nanoparticles. Coating, modification, and characterization, *Mater. Chem. Phys.*, 2018, **205**, 113–119, DOI: 10.1016/j.matchemphys.2017.11.009.

62 C. S. Xavier, C. A. Paskocimas, F. V. da Motta, V. D. Araújo, M. J. Aragón, J. L. Tirado, P. Lavela, E. Longo and M. R. B. Delmonte, Microwave-assisted hydrothermal synthesis of magnetite nanoparticles with potential use as anode in lithium ion batteries, *Mater. Res.*, 2014, **17**, 1065–1070, DOI: 10.1590/1516-1439.264714.

63 G. Zambzickaite, M. Talaikis, J. Dobilas, V. Stankevic, A. Drabavicius, G. Niaura and L. Mikoliunaite, Microwave-Assisted Solvothermal Synthesis of Nanocrystallite-Derived Magnetite Spheres, *Materials*, 2022, **15**, 4008–4023, DOI: 10.3390/ma15114008.

64 D.-S. Kotoulas, K. Angelakeris, A. Kotoulas, C. Dendrinou-Samara, M. Angelakeris and O. Kalogirou, The Effect of Polyol Composition on the Structural and Magnetic Properties of Magnetite Nanoparticles for Magnetic Particle Hyperthermia, *Materials*, 2019, **12**, 2663–2688, DOI: 10.3390/ma12172663.

65 E. C. Vreeland, J. Watt, G. B. Schober, B. G. Hance, M. J. Austin, A. D. Price, B. D. Fellows, T. C. Monson, N. S. Hudak, L. Maldonado-Camargo, A. C. Bohorquez, C. Rinaldi and D. L. Huber, Enhanced Nanoparticle Size Control by Extending LaMer's Mechanism, *Chem. Mater.*, 2015, **27**, 6059–6066, DOI: 10.1021/acs.chemmater.5b02510.

66 W. Ostwald, Über die vermeintliche Isomerie des roten und gelben Quecksilberoxyds und die Oberflächenspannung fester Körper, *Z. Phys. Chem.*, 1900, **34**, 495–503, DOI: 10.1515/zpch-1900-3431.

67 K. E. J. Lehtinen and M. R. Zachariah, Energy accumulation in nanoparticle collision and coalescence processes, *J. Aerosol Sci.*, 2002, **33**, 357–368, DOI: 10.1016/S0021-8502(01)00177-X.

68 T. Fan, D. Pan and H. Zhang, Study on formation mechanism by monitoring the morphology and structure evolution of nearly monodispersed Fe3O4 submicroparticles with controlled particle sizes, *Ind. Eng. Chem. Res.*, 2011, **50**, 9009–9018, DOI: 10.1021/ie200970j.

69 W. Wu, Z. Wu, T. Yu, C. Jiang and W.-S. S. Kim, Recent progress on magnetic iron oxide nanoparticles: synthesis, surface functional strategies and biomedical applications, *Sci. Technol. Adv. Mater.*, 2015, **16**, 023501–023543, DOI: 10.1088/1468-6996/16/2/023501.

70 J. Fock, L. K. Bogart, D. González-Alonso, J. I. Espeso, M. F. Hansen, M. Varón, C. Frandsen and Q. A. Pankhurst, On the 'centre of gravity' method for measuring the composition of magnetite/maghemite mixtures, or the stoichiometry of magnetite-maghemite solid solutions, via 57 Fe Mössbauer spectroscopy, *J. Phys. D Appl. Phys.*, 2017, **50**, 265005–265020, DOI: 10.1088/1361-6463/aa73fa.

71 R. Hiraga, O. da F. M. Gomes and R. Neumann, Maghemite in brazilian iron ores: Quantification of the magnetite-maghemite isomorphic series by x-ray diffraction and the rietveld method, and confirmation by independent methods, *Minerals*, 2021, **11**, 346–364, DOI: 10.3390/min11040346.

72 W. Kim, C.-Y. Suh, S.-W. Cho, K.-M. Roh, H. Kwon, K. Song and I.-J. Shon, A new method for the identification and quantification of magnetite–maghemite mixture using conventional X-ray diffraction technique, *Talanta*, 2012, **94**, 348–352, DOI: 10.1016/j.talanta.2012.03.001.

73 S. J. Iyengar, M. Joy, C. K. Ghosh, S. Dey, R. K. Kotnala and S. Ghosh, Magnetic, X-ray and Mössbauer studies on magnetite/maghemite core–shell nanostructures fabricated through an aqueous route, *RSC Adv.*, 2014, **4**, 64919–64929, DOI: 10.1039/C4RA11283K.

74 K. Nakamoto, *Infrared and Raman Spectra of Inorganic and Coordination Compounds*, 6th edn, Wiley, Hoboken, NJ, USA, 2008, DOI: 10.1002/9780470405840.

75 M. Chirea, A. Freitas, B. S. Vasile, C. Ghitulica, C. M. Pereira and F. Silva, Gold Nanowire Networks: Synthesis, Characterization, and Catalytic Activity, *Langmuir*, 2011, **27**, 3906–3913, DOI: 10.1021/la104092b.

76 U. Sharma, B. Tyagi and R. V. Jasra, Synthesis and Characterization of Mg–Al–CO3 Layered Double Hydroxide for CO2 Adsorption, *Ind. Eng. Chem. Res.*, 2008, **47**, 9588–9595, DOI: 10.1021/ie800365t.

77 D. G. Evans and R. C. T. Slade, Structural Aspects of Layered Double Hydroxides, in *Structure Bonding*, D. G. Duan and X., Evans, 119th edn, Springer, Berlin, Heidelberg, 2005, pp. 1–87, DOI: 10.1007/430_005.

78 G. S. Machado, F. Wypych and S. Nakagaki, Anionic iron(III) porphyrins immobilized on zinc hydroxide chloride as catalysts for heterogeneous oxidation reactions, *Appl. Catal., A*, 2012, **413–414**, 94–102, DOI: 10.1016/j.apcata.2011.10.046.

79 G. G. C. Arízaga, K. G. Satyanarayana and F. Wypych, Layered hydroxide salts: Synthesis, properties and potential applications, *Solid State Ionics*, 2007, **178**, 1143–1162, DOI: 10.1016/j.ssi.2007.04.016.

80 F. Wypych, G. A. A. Bubniak, M. Halma and S. Nakagaki, Exfoliation and immobilization of anionic iron porphyrin in layered double hydroxides, *J. Colloid Interface Sci.*, 2003, **264**, 203–207, DOI: 10.1016/S0021-9797(03)00374-6.

81 J. H. Choy, S. J. CHOI, J. M. OH and T. Park, Clay minerals and layered double hydroxides for novel biological applications, *Appl. Clay Sci.*, 2007, **36**, 122–132, DOI: 10.1016/j.clay.2006.07.007.
82 K. Kannan, J. Mukherjee, P. Mishra and M. N. Gupta, Nickel Ferrite Nanoparticles as an Adsorbent for Immobilized Metal Affinity Chromatography of Proteins, *J. Chromatogr. Sci.*, 2021, **59**, 262–268, DOI: 10.1093/chromsci/bmaa102.
83 D. K. Dinkar, B. Das, R. Gopalan and B. S. Dehiya, Magnetic and optical properties of green synthesized nickel ferrite nanoparticles and its application into photocatalysis, *Nanotechnology*, 2021, **32**, 505725–505736, DOI: 10.1088/1361-6528/ac24c2.
84 A. Mandziak, J. de la Figuera, S. Ruiz-Gómez, G. D. Soria, L. Pérez, P. Prieto, A. Quesada, M. Foerster and L. Aballe, Structure and magnetism of ultrathin nickel-iron oxides grown on Ru(0001) by high-temperature oxygen-assisted molecular beam epitaxy, *Sci. Rep.*, 2018, **8**, 17980–17987, DOI: 10.1038/s41598-018-36356-6.
85 X. Xu, M. Ge, C. Wang and J. Z. Jiang, High temperature stable monodisperse superparamagnetic core-shell iron-oxide@SnO2 nanoparticles, *Appl. Phys. Lett.*, 2009, **95**, 183112–183114, DOI: 10.1063/1.3261756.
86 K. Zhang, M. Davis, J. Qiu, L. Hope-Weeks and S. Wang, Thermoelectric properties of porous multi-walled carbon nanotube/polyaniline core/shell nanocomposites, *Nanotechnology*, 2012, **23**, 385701–385708, DOI: 10.1088/0957-4484/23/38/385701.
87 X. Bi, T. Fan and H. Zhang, Novel morphology-controlled Hierarchical core@shell structural organo-layered double hydroxides magnetic nanovehicles for drug release, *ACS Appl. Mater. Interfaces*, 2014, **6**, 20498–20509, DOI: 10.1021/am506113s.
88 T. K. Jain, M. A. Morales, S. K. Sahoo, D. L. Leslie-Pelecky and V. Labhasetwar, Iron oxide nanoparticles for sustained delivery of anticancer agents, *Mol. Pharm.*, 2005, **2**, 194–205, DOI: 10.1021/mp0500014.
89 M. Gouterman, L. Bajema, M. Gouterman and B. Meyer, Spectra of porphyrins, *J. Mol. Spectrosc.*, 1961, **6**, 138–163, DOI: 10.1016/0022-2852(61)90236-3.
90 J. R. Lindsay Smith, Y. Iamamoto and F. S. Vinhado, Oxidation of alkanes by iodosylbenzene (PhIO) catalysed by supported Mn(III) porphyrins: Activity and mechanism, *J. Mol. Catal. A: Chem.*, 2006, **252**, 23–30, DOI: 10.1016/j.molcata.2006.01.064.
91 G. S. Machado, K. A. D. F. Castro, F. Wypych and S. Nakagaki, Immobilization of metalloporphyrins into nanotubes of natural halloysite toward selective catalysts for oxidation reactions, *J. Mol. Catal. A: Chem.*, 2008, **283**, 99–107, DOI: 10.1016/j.molcata.2007.12.009.
92 A. L. Stevens, N. K. Joshi, M. F. Paige and R. P. Steer, Photophysics of Zinc Porphyrin Aggregates in Dilute Water–Ethanol Solutions, *J. Phys. Chem. B*, 2017, **121**, 11180–11188, DOI: 10.1021/acs.jpcb.7b09868.
93 K. M. Mantovani, K. C. Molgero Westrup, R. M. da Silva Junior, S. Jaerger, F. Wypych and S. Nakagaki, Oxidation catalyst obtained by the immobilization of layered double hydroxide/Mn(III) porphyrin on monodispersed silica spheres, *Dalt. Trans.*, 2018, **47**, 3068–3073, DOI: 10.1039/C7DT03656F.
94 B. P. Borah, S. Majumder, K. D. Borah and J. Bhuyan, The quest for a better understanding of ethanol coordination to magnesium and zinc porphyrin: A combined experimental and theoretical study, *J. Mol. Struct.*, 2021, **1230**, 129646–129654, DOI: 10.1016/j.molstruc.2020.129646.
95 M. A. Fodor, P. Szabó, G. Lendvay and O. Horváth, Characterization of the UV-Visible absorption spectra of manganese(III) porphyrins with time-dependent density functional theory calculations, *Z. Phys. Chem.*, 2022, **236**, 27–51, DOI: 10.1515/zpch-2020-1787.
96 G. M. Ucoski, K. A. D. F. Castro, K. J. Ciuffi, G. P. Ricci, J. A. Marques, F. S. Nunes and S. Nakagaki, Use of iron and manganese porphyrins in solution and immobilized on silica obtained by the sol–gel process as catalyst in the oxidation of organic substrates, *Appl. Catal., A*, 2011, **404**, 120–128, DOI: 10.1016/j.apcata.2011.07.019.
97 S. Nakagaki, K. A. D. F. Castro, G. S. Machado, M. Halma, S. M. Drechsel and F. Wypych, Catalytic activity in oxidation reactions of anionic iron(III) porphyrins immobilized on raw and grafted chrysotile, *J. Braz. Chem. Soc.*, 2006, **17**, 1672–1678, DOI: 10.1590/S0103-50532006000800027.
98 S. Nakagaki, M. Halma, A. Bail, G. G. C. Arízaga and F. Wypych, First insight into catalytic activity of anionic iron porphyrins immobilized on exfoliated layered double hydroxides, *J. Colloid Interface Sci.*, 2005, **281**, 417–423, DOI: 10.1016/j.jcis.2004.08.098.
99 S. A. Maruyama, K. C. M. Westrup, S. Nakagaki and F. Wypych, Immobilization of a cationic manganese(III) porphyrin on lithium gordaite (LiZn4(OH)6(SO4)Cl·6H2O), a layered hydroxide salt with cation exchange capacity, *Appl. Clay Sci.*, 2017, **139**, 108–111, DOI: 10.1016/j.clay.2017.01.010.
100 U. Junghans, C. Suttkus, J. Lincke, D. Lässig, H. Krautscheid and R. Gläser, Selective oxidation of cyclooctene over copper-containing metal-organic frameworks, *Microporous Mesoporous Mater.*, 2015, **216**, 151–160, DOI: 10.1016/j.micromeso.2015.01.050.
101 D. R. Leanord and J. R. L. Smith, Model systems for cytochrome P450 dependent mono-oxygenases. Part 7. Alkene epoxidation by iodosylbenzene catalysed by ionic iron(III) tetraarylporphyrins supported on ion-exchange resins, *J. Chem. Soc., Perkin Trans.*, 1990, **2**, 1917–1923, DOI: 10.1039/P29900001917.
102 B. Meunier, S. P. de Visser and S. Shaik, Mechanism of Oxidation Reactions Catalyzed by Cytochrome P450 Enzymes, *Chem. Rev.*, 2004, **104**, 3947–3980, DOI: 10.1021/cr020443g.
103 G. S. Machado, F. Wypych and S. Nakagaki, Immobilization of anionic iron(III) porphyrins onto in situ obtained zinc oxide, *J. Colloid Interface Sci.*, 2012, **377**, 379–386, DOI: 10.1016/j.jcis.2012.03.083.

104 D. Sun, Z. Wu, X. Zhang, J. Yang, Y. Zhao, W. Nam and Y. Wang, Brønsted Acids Promote Olefin Oxidations by Bioinspired Nonheme Co III (PhIO)(OH) Complexes: A Role for Low-Barrier Hydrogen Bonds, *J. Am. Chem. Soc.*, 2023, **145**, 5739–5749, DOI: 10.1021/jacs.2c12307.

105 S. Das, J. Pérez-Ramírez, J. Gong, N. Dewangan, K. Hidajat, B. C. Gates and S. Kawi, Core–shell structured catalysts for thermocatalytic, photocatalytic, and electrocatalytic conversion of CO 2, *Chem. Soc. Rev.*, 2020, **49**, 2937–3004, DOI: 10.1039/C9CS00713J.

106 D. Mansuy, J. Leclaire, M. Fontecave and P. Dansette, Regioselectivity of olefin oxidation by iodosobenzene catalyzed by metalloporphyrins : control by the catalyst, *Tetrahedron*, 1984, **40**, 2847–2857, DOI: 10.1016/S0040-4020(01)91293-1.

107 J. T. Groves, T. E. Nemo and R. S. Myers, Hydroxylation and epoxidation catalyzed by iron-porphine complexes. Oxygen transfer from iodosylbenzene, *J. Am. Chem. Soc.*, 1979, **101**, 1032–1033, DOI: 10.1021/ja00498a040.

108 W. Nam and J. S. Valentine, Zinc(II) complexes and aluminum(III) porphyrin complexes catalyze the epoxidation of olefins by iodosylbenzene, *J. Am. Chem. Soc.*, 1990, **112**, 4977–4979, DOI: 10.1021/ja00168a063.

109 S. Nakagaki, G. K. B. Ferreira, G. Ucoski and K. A. D. F. Castro, Chemical Reactions Catalyzed by Metalloporphyrin-Based Metal-Organic Frameworks, *Molecules*, 2013, **18**, 7279–7308, DOI: 10.3390/molecules18067279.